Simulations of the flow in the Mahakam river–lake–delta system, Indonesia

Pham Van, Chien; de Brye, Benjamin; Deleersnijder, Eric; Hoitink, A. J F; Sassi, Maximiliano; Spinewine, Benoit; Hidayat, Hidayat; Soares-Frazão, Sandra

DOI
10.1007/s10652-016-9445-4

Publication date
2016

Document Version
Accepted author manuscript

Published in
Environmental Fluid Mechanics

Accepted for publication in "Environmental Fluid Mechanics"
(7th January 2016)

Simulations of the flow in the Mahakam river-lake-delta system, Indonesia

Chien Pham Van[1, 2,*], Benjamin de Brye[3], Eric Deleersnijder[4,5], A.J.F. (Ton) Hoitink[6], Maximiliano Sassi[7], Benoit Spinewine[1], Hidayat Hidayat[6], and Sandra Soares-Frazão[1]

[1]Université catholique de Louvain, Institute of Mechanics, Materials and Civil Engineering (IMMC), Place du Levant 1, Louvain-la-Neuve, Belgium.

[2]Thuyloi University, Faculty of Hydrology and Water Resources, Tayson 175, Dongda District, Hanoi, Viet Nam.

[3]Free Field Technologies, Axis Park Louvain-la-Neuve, rue Emile Francqui 1, Mont-Saint-Guibert, Belgium.

[4]Université catholique de Louvain, Institute of Mechanics, Materials and Civil Engineering (IMMC) & Earth and Life Institute (ELI), Avenue Georges Lemaître 4, Louvain-la-Neuve, Belgium.

[5]Delft University of Technology, Delft Institute of Applied Mathematics (DIAM), Mekelweg 4, 2628 CD Delft, The Netherlands

[6]Wageningen University, Department of Environmental Sciences, Hydrology and Quantitative Water Management Group, Droevendaalsesteeg 3, Wageningen, The Netherlands.

[7]Royal Netherlands Institute for Sea Research, NIOZ, Den Burg, The Netherlands.

[*]**Corresponding author:** Tel.: +32/10/472124, Fax.: +32/10/472179, Email.: chien.phamvan@uclouvain.be or Pchientvct_tv@tlu.edu.vn

Abstract

Large rivers often present a river-lake-delta system, with a wide range of temporal and spatial scales of the flow due to the combined effects of human activities and various natural factors, e.g. river discharge, tides, climatic variability, droughts, floods. Numerical models that allow for simulating the flow in these river-lake-delta systems are essential to study them and predict their evolution under the impact of various forcings. This is because they provide information that cannot be easily measured with sufficient temporal and spatial detail. In this study, we combine one-dimensional sectional-averaged (1D) and two-dimensional depth-averaged (2D) models, in the framework of the finite element model SLIM, to simulate the flow in the Mahakam river-lake-delta system (Indonesia). The 1D model representing the Mahakam River and four tributaries is coupled to the 2D unstructured mesh model implemented on the Mahakam Delta, the adjacent Makassar Strait, and three lakes in the central part of the river catchment. Using observations of water elevation at five stations, the bottom friction for river and tributaries, lakes, delta, and adjacent coastal zone is calibrated. Next, the model is validated using another period of observations of water elevation, flow velocity, and water discharge at various stations. Several criteria are implemented to assess the quality of the simulations, and a good agreement between simulations and observations is achieved in both calibration and validation stages. Different aspects of the flow, i.e. the division of water at two bifurcations in the delta, the effects of the lakes on the flow in the lower part of the system, the area of tidal propagation, are also quantified and discussed.

Keywords

Mahakam River, coupled 1D / 2D model, SLIM, river-lake-delta system

1 Introduction

Large rivers such as the Mekong River (Southeast Asia) hosting a river-lake-delta system consist of various interconnected regions such as a river and its tributaries, lakes, floodplains, delta or estuary, and adjacent coastal ocean. In such river-lake-delta systems, continuous interactions and exchange of water between interconnected regions exist, under the combined effects of riverine and marine forcings (e.g. river discharge, tides), mutual influences of natural processes (e.g. climatic variability, droughts, floods), and human activities [1,2]. As a results, a wide range of temporal and spatial scales of motion can be observed [2]. Such systems also feature complex geometries, especially in deltaic or estuarine regions [2,3]. Therefore, a global system approach that is able to handle the flow in the whole river-lake-delta system is required, to understand the complex flow processes occurring at different temporal and spatial scales and to study related issues, e.g. transport processes of sediment, morphology, ecological status of coastal waters.

Detailed and long-term field measurements (e.g. flow velocity, flow depth, water discharge) allow for an accurate study of the flow, but are generally time-consuming and rarely obtained over long time intervals and at different locations due to the highly spatial and temporal variability of the phenomena. As regards numerical simulations, an integrated model, which allows for representing the flow from the upstream end of the system to the coastal ocean and the deep margin, is essential to take into account properly the interactions between river flow, hydraulic processes, and tidal effects on the entire river-lake-delta systems. While existing studies primarily investigate the flow processes locally in each interconnected region of river-lake-delta systems, taken individually, it is becoming computationally feasible to adopt such an integrated approach, without excessive simplification of the physical processes resolved by the model.

Using a full three-dimensional (3D) model for simulating the flow in river-lake-delta systems is however likely to exceed the available computer resources because the area of such systems is of the order of thousands of square kilometers. The data required to run such models are also not easily available, as well as field measurements to validate the implementation of the model. Among

different simpler models developed for simulating the flow in riverine and marine water environments as well as in continuums such as river-lake-delta systems, a coupled one-dimensional section-averaged and two-dimensional depth-averaged (1D / 2D) model is a tool of choice, for it is more efficient in terms of computational cost than a full 2D or 3D model [3-7].

Wu and Li [4] applied a coupled 1D / 2D quasi-steady model to study the flow in the fluctuating backwater region of the Yangtze River while Zhang [5] used a 1D / 2D unsteady model to simulate the flow in the offshore area near the Yellow River mouth (China). Martini *et al*. [6] applied a coupled 1D / 2D model for simulating the flood flows in the Brenta River (Veneto, Italy). Later, Cook and Merwade [7] combined the simulation results from a coupled 1D / 2D model and datasets obtained from different river bathymetry sources in order to quantify the resulting differences in the inundation maps for Strouds Creek reach and Brazos River (USA). Recently, de Brye *et al*. [3] developed a coupled 1D / 2D finite element model for reproducing the flow dynamics in the Scheldt Estuary and tidal river network. These examples strongly suggest that a coupled 1D / 2D model can be used to reproduce the flow in river-lake-delta systems.

In the framework of a coupled 1D / 2D model, the 2D model is often developed in the part of the domain of interest, e.g. delta or estuary, where the accurate representation of the topography and complex coastlines is required. In this 2D calculation area, different numerical methods and grids were used, for example, finite difference method by Wu and Li [4] and Zhang [5], finite element method and structured mesh by Cook and Marwade [7], finite element method and an unstructured mesh by Martini *et al*. [6] and de Brye *et al*. [3]. Finite-element or finite-volume models using unstructured meshes constitute a promising option to deal with the multi-physics and multi-scale features of the problem [8,9], especially in deltaic and estuarine regions exhibiting a large number of narrow channels [3]. This is because unstructured meshes allow for a more accurate representation of complex topographies and an increase in spatial resolution in areas of interest, as was done, for example, in the simulations of the flow in the Great Barier Reef [10].

The present study aims at (i) applying an existing unstructured-mesh, finite element model, i.e.

SLIM (www.climate.be/slim), in which one-dimensional sectional-averaged and two-dimensional depth-averaged shallow-water equations are coupled, to simulate the flow in the Mahakam river-lake-delta system, (ii) accurately reproducing the observations of the flow (i.e. water elevation, flow velocity, and water discharge) at various locations in the system, (iii) investigating the division of water at two bifurcations in the deltaic region, (iv) providing a preliminary investigation of the effects of the lakes on the flow in the lower part of the system, and (v) identifying the area of tidal propagation in the system. Besides these objectives, the study also allowed to represent the numerous distributaries in the deltaic region with a refined accuracy and to determine appropriate values of the bottom friction coefficients in different parts of the considered river-lake-delta system.

The paper first introduces the Mahakam river-lake-delta system. Then, the finite element model used in the study and the model established for the studied system are described. The detailed calibration procedure of the modelling parameters and the validation of the model using available observations of the flow (e.g. water elevation, flow velocity, and water discharge) are also presented before discussing related issues, e.g. effects of grid resolution. Finally, conclusions are drawn.

2 The Mahakam river-lake-delta system

The Mahakam River is located in the East Kalimantan province of Borneo, Indonesia (Fig. 1). The river-lake-delta system consists of the Mahakam River and its tributaries, lakes, the Mahakam Delta, and the adjacent Makassar Strait. The river meanders over 900 km and its catchment area covers about 75,000 km^2, with a mean annual river discharge of the order of 3,000 m^3/s [11]. The river is characterized by a tropical rain forest climate with a dry season from May to September and a wet season from October to April. In the river catchment, the mean daily temperature varies from 24 to 29^oC while the relative humidity lies between 77 and 99% [12]. The mean annual rainfall varies between 4,000 and 5,000 mm/year in the central highlands and decreases from 2,000 to 3,000 mm/year near the coast [13]. A bimodal rainfall pattern with two peaks of rainfall occurring generally in December and May is reported in the river catchment [12]. Due to the regional climate and the global air circulation, the hydrological conditions in the river catchment vary significantly,

especially in ENSO (El Nino-Southern Oscillation) years such as in 1997, leading to significant variations of flow in the river and downstream region, i.e. the delta [12].

In the middle part of the Mahakam River catchment, there are four tributaries (i.e. Kedang Pahu, Belayan, Kedang Kepala, and Kedang Rantau) and over thirty shallow-water lakes covering a total area of about 400 km^2. These lakes are connected to the Mahakam River system through small channels (Fig. 1). The water collected over vast regions of the land around these lakes can be stored in the lakes. Obviously, the water from the connected channels can flow into or out of the lakes, depending on the season, e.g. flood or drought periods. For instance, these lakes act as a buffer of the Mahakam River and regulate the water discharge in the lower part of the river through the damping of flood surges [14]. During the dry season, tides can also force a flow into the lakes. Therefore, studies of the flow in the Mahakam river-lake-delta system have to take into account the interconnections between these lakes and the river.

Downstream of the Mahakam River, the Mahakam Delta presents a multi-channel network including a large number of active distributaries and tidal channels. The delta is symmetrical with a radius of approximately 50 km, as measured from the delta shore to the delta apex. The width of the channels in the deltaic region ranges from 10 m to 3 km. The delta discharges into the Makassar Strait, whose width varies between 200 and 300 km, with a length of about 600 km. Located between the islands of Borneo and Sulawesi, the Makassar Strait is the main passage for the transfer of water and heat from the Pacific to the Indian Ocean by the Indonesian Throughflow [15,16].

Complex coastlines are present in the delta (Fig. 1). Such complex coastlines might have a significant impact on the flow [17]. This means that the effects of complex coastlines have to be taken into account in studies of the flow. In addition, because of the multi-channel network, many bifurcations are also inherently exhibited in the delta. Division of water discharge at these bifurcations should be accurately represented since it affects not only the flow dynamics [2] but also the sediment distribution and morphology in the adjacent channels [18].

The Mahakam Delta is a mixed tidal and fluvial delta. The tide in the delta is dominated by

semidiurnal and diurnal regimes, with a predominantly semidiurnal one. The tidal range decreases from the delta front to upstream Mahakam River and its value varies between 3 and 1 m, depending on the location and the tidal phase (e.g. neap or spring tides) under consideration.

Partial mixing is reported in the delta, based on the vertical distribution of salinity collected at different locations [14]. The limit of salt intrusion is located around the delta apex [14,19,20]. Temperature data collection at 29 locations in the whole delta [20] shows that the temperature varies from 29.2 to 30.5^{o}C at the surface and from 29.2 to 30.8^{o}C at the bottom. This suggests that there is no large difference of water temperature in the water column and between stations for different tidal conditions.

Large parts of the open waters in the delta are sheltered from wind action by vegetation and thus the influence of the wind will not be taken into account in the calculations presented hereinafter. The effect of wind on the flow in the lakes is also disregarded, mainly because there are not available wind data in this region. In the Makassar Strait, the effect of the wind is limited due to low-level wind speed. In terms of wind-induced surface waves, the average wave height is about 0.3 m at a distance of 14 km offshore and the maximum wave height is less than 0.6 m with the largest waves approaching from the southeast [21]. Due to the limited fetch in the narrow strait of the Makassar and low-level wind speed, the mean value of the significant wave height is also less than 0.6 m and the wave energy that affects the deltaic processes is very small [14]. Therefore, the effects of wind and waves are assumed to be negligible in this study.

3 Model

3.1 Governing equations

The two-dimensional depth-averaged shallow-water equations are applied in the Mahakam Delta, lakes, and the Makassar Strait. The elevation η of the water surface above the reference level and the depth-averaged horizontal velocity vector $\mathbf{u} = (u, v)$ are obtained by solving the following equations:

$$\frac{\partial \eta}{\partial t} + \nabla \cdot \left(H\mathbf{u} \right) = 0 \tag{1}$$

$$\frac{\partial \mathbf{u}}{\partial t} + \mathbf{u} \cdot \left(\nabla \mathbf{u} \right) + f\mathbf{k} \times \mathbf{u} + \mathrm{g}\nabla \eta = \frac{1}{H} \nabla \cdot \left[H\nu \left(\nabla \mathbf{u} \right) \right] - \frac{\boldsymbol{\tau}_\mathbf{b}}{\rho H} \tag{2}$$

where t is the time and ∇ is the horizontal del operator; $H = \eta + h$ is the water depth, with h being the water depth below the reference level (taken as the mean sea level); $f = 2\omega\sin\phi$ is the Coriolis parameter, ω is the Earth's angular velocity and ϕ is the latitude, $\mathbf{k}$ is the unit upward vector; g is the gravitational acceleration; ρ is the water density (assumed constant); ν is the horizontal eddy viscosity; $\boldsymbol{\tau}_\mathbf{b}$ is the bottom shear stress, which is parameterized using the Manning-Strickler formulation:

$$\boldsymbol{\tau}_\mathbf{b} = \rho \frac{\mathrm{g}n^2 \left\| \mathbf{u} \right\|}{H^{1/3}} \mathbf{u} \tag{3}$$

where n is the Manning coefficient, generally depending on the physical properties of the riverbed and the seabed. Basically, the value of n is calibrated in order to reproduce the flow as well as possible.

The eddy viscosity ν is evaluated using the Smagorinsky formula [22]:

$$\nu = \left(0.1\Delta \right)^2 \sqrt{2\left(\frac{\partial u}{\partial x} \right)^2 + \left(\frac{\partial u}{\partial y} + \frac{\partial v}{\partial x} \right)^2 + 2\left(\frac{\partial v}{\partial y} \right)^2} \tag{4}$$

where Δ is the local characteristic length scale of the element, i.e. the longest edge of a triangle in the 2D unstructured mesh. The Smagorinsky formula arises from the unresolved turbulence at the subgrid scale and depends on the strain-rate of the velocity field. The energy production and dissipation of the small scales are assumed to be in equilibrium in this formula.

The continuity and momentum equations are integrated over the river cross-section in the Mahakam River and tributaries, yielding the following one-dimensional equations

$$\frac{\partial A}{\partial t} + \frac{\partial \left(Au \right)}{\partial x} = 0 \tag{5}$$

$$\frac{\partial u}{\partial t} + u\frac{\partial u}{\partial x} + \mathrm{g}\frac{\partial \eta}{\partial x} = \frac{1}{A}\frac{\partial}{\partial x}\left(\nu A \frac{\partial u}{\partial x} \right) - \frac{\tau_\mathrm{b}}{\rho H} \tag{6}$$

where A is the cross-sectional area, $H = A/b$ is the effective water depth, and b is the river width. The bottom shear stress τ_b in the 1D model is computed using Manning's formula as:

$$\tau_b = \rho \frac{g n^2 |u|}{H^{1/3}} u. \quad (7)$$

The eddy viscosity is parameterized using the zero-equation turbulent model [23], under the form:

$$\nu = 0.16 u_* H \quad (8)$$

where u_* is the shear velocity, which is calculated as $u_*^2 = c_f u^2$, with c_f being a coefficient obtained from Manning's formula ($c_f = g n^2 H^{-1/3}$).

3.2 Wetting and drying algorithm

In the river-lake-delta system and particular in the deltaic region, several areas can be wet or dry depending on the water elevation and tidal conditions. An accurate representations of these wetting / drying areas is crucial and mandatory in any model aimed at reproducing the flow in such systems. In this paper, we use the wetting and drying algorithm designed by Kärnä *et al*. [24]. This means that the actual bathymetry (i.e. the water depth h below the reference level) is modified according to a smooth function $f(H)$ as $h_m = h + f(H)$, to ensure a positive water thickness at any time. The smooth function has to satisfy the following properties. Firstly, the modified water depth (i.e. $H_m = h_m + \eta$) is positive at any time and position. Secondly, the difference between the real and modified water depths is negligible when the water depth is significantly positive. Thirdly, the smooth function is continuously differentiable to ensure convergence of Newton iterations when using an implicit time stepping. The following function, which satisfies the properties described above, is used:

$$f(H) = \frac{1}{2}\left(\sqrt{H^2 + \xi^2} - H\right) \quad (9)$$

where ξ is a free parameter controlling the smoothness of the transition between dry and wet situations, with the smaller value of ξ corresponding to the smaller the transition zone [24]. The modified water depth, i.e. $H_m = h_m + \eta$ will be equal to $\xi/2$ when $H = 0$, revealing that ξ also directly controls the water depth in the dry area. In our calculations, a value $\xi = 0.5$ m is adopted for modifying the bathymetry, in order to maintain the positive water depth.

Using the redefined total water depth, the depth-averaged shallow-water equations (1)-(2) are

191 modified slightly, resulting in the following forms:

$$\frac{\partial \eta}{\partial t} + \frac{\partial h_m}{\partial t} + \nabla \cdot \left(H_m \mathbf{u} \right) = 0 \tag{10}$$

$$\frac{\partial \mathbf{u}}{\partial t} + \mathbf{u} \cdot \left(\nabla \mathbf{u} \right) + f\mathbf{k} \times \mathbf{u} + g\nabla \eta = \frac{1}{H_m} \nabla \cdot \left[H_m \nu \left(\nabla \mathbf{u} \right) \right] - \frac{\boldsymbol{\tau}_b}{\rho H_m} \cdot \tag{11}$$

192 The appearance of the second term in eq. (10) is due to the redefinition of the bathymetry.

193 ### 3.3 Finite element implementation

194 The governing equations (5)-(6) and (10)-(11) are solved by means of an implicit discontinuous
195 Galerkin finite element method (DG-FEM) in the framework of the unstructured-mesh, finite
196 element model SLIM (www.climate.be/slim, [3,24,25]). To avoid a repeated description of the
197 model and its capabilities, only general information about the finite element (FE) implementation of
198 these equation is presented below. The computational domain is discretized into triangle elements
199 and line segments as shown in Fig. 4. The governing equations are multiplied by test functions and
200 then integrated by parts over each element or segment, resulting in element-wise surface and
201 contour integral terms for the spatial operators. The surface term is estimated using a linear shape
202 function. An approximate Riemann solver is used for computing the fluxes at the interfaces between
203 two adjacent elements or segments in order to represent properly the water-wave dynamics in
204 contour terms [25]. A second-order diagonally implicit Runge-Kutta method is used for the
205 temporal derivative operator [24] and a time step of 10 minutes is used in this study. At the
206 interfaces between the 1D and 2D models, the local conservation is guaranteed by compatible one
207 and two dimensional numerical fluxes [3].

208 ### 3.4 Treatment of channel confluences in the 1D model

209 To impose suitable conditions at the interface of a confluence point (where waters in two channels
210 flow into a single channel) in the Mahakam River, a special treatment is needed because of the
211 following reasons. Firstly, one computational confluence node is associated with three nodal values
212 and the usual Riemann solver [40] cannot be resorted to compute the numerical fluxes at the
213 interface of a confluence node. Secondly, a confluence node can be handled rather easily in
214 conservative finite difference models, but not in finite element ones [26]. In this study, we

implemented a method inspired by Sherwin *et al*. [26] for arterial systems. This means that the characteristic variables are used to compute the fluxes at the interface of the confluence point, together with the continuity of mass and momentum. The detailed derivation of these characteristic variables from the governing equations is described below. The governing equations (5) and (6) can be expressed in a vector form as

$$\frac{\partial \mathbf{U}}{\partial t} + \mathbf{A}\frac{\partial \mathbf{U}}{\partial x} = \mathbf{S} \tag{12}$$

where $\mathbf{U} = \begin{pmatrix} A \\ u \end{pmatrix}$, $\mathbf{A} = \begin{pmatrix} u & A \\ g/b & u \end{pmatrix}$, $\mathbf{S} = \begin{pmatrix} 0 \\ \frac{1}{A}\frac{\partial}{\partial x}\left(\nu A \frac{\partial u}{\partial x}\right) - \frac{\tau_b}{\rho H} \end{pmatrix}$.

The eigenvalues of the eq. (12) can be easily obtained by solving the equation $\det(\mathbf{A} - \lambda\mathbf{I}) = 0$. The eigenvalues, λ_1 and λ_2, are real:

$$\lambda_1 = u + \sqrt{\frac{gA}{b}} \quad \text{and} \quad \lambda_2 = u - \sqrt{\frac{gA}{b}}. \tag{13}$$

The characteristic variables **W** can be determined by using the expression $\mathbf{W}=\mathbf{K}^{-1}\mathbf{U}$, with **K** being the eigenmatrix whose elements are determined from the eigenvalues:

$$\mathbf{K} = \begin{pmatrix} 1 & 1 \\ \sqrt{\frac{g}{Ab}} & -\sqrt{\frac{g}{Ab}} \end{pmatrix}. \tag{14}$$

Finally, the characteristic variables **W** are obtained:

$$\mathbf{W} = \begin{bmatrix} \frac{1}{2}\left(A + u\sqrt{\frac{Ab}{g}}\right) \\ \frac{1}{2}\left(A - u\sqrt{\frac{Ab}{g}}\right) \end{bmatrix}. \tag{15}$$

Because the discontinuous Galerkin method is applied at a confluence point, one computational confluence node is associated with 3 nodal values (Fig. 2) and thus six unknowns, i.e. sectional area and velocity of each node. If these six variables (A_l, u_l, A_{r1}, u_{r1}, A_{r2}, and u_{r2}) at the interface are known, we can compute the six upwind variables (A_{ul}, u_{ul}, A_{ur1}, u_{ur1}, A_{ur2}, and u_{ur2}) by imposing the characteristic variables from eq. (15) and by using the continuity of mass and momentum fluxes at the confluence. The characteristic variables at the interfaces of the confluence point are assumed to remain constant:

$$\frac{1}{2}\left(A_l+u_l\sqrt{\frac{A_l b_l}{\mathrm{g}}}\right)=\frac{1}{2}\left(A_{ul}+u_{ul}\sqrt{\frac{A_{ul}b_l}{\mathrm{g}}}\right) \tag{16}$$

$$\frac{1}{2}\left(A_{r1}-u_{r1}\sqrt{\frac{A_{r1}b_{r1}}{\mathrm{g}}}\right)=\frac{1}{2}\left(A_{ur1}-u_{ur1}\sqrt{\frac{A_{ur1}b_{r1}}{\mathrm{g}}}\right) \tag{17}$$

$$\frac{1}{2}\left(A_{r2}-u_{r2}\sqrt{\frac{A_{r2}b_{r2}}{\mathrm{g}}}\right)=\frac{1}{2}\left(A_{ur2}-u_{ur2}\sqrt{\frac{A_{ur2}b_{r2}}{\mathrm{g}}}\right) \tag{18}$$

$$A_{ul}u_{ul}=A_{ur1}u_{ur1}+A_{ur2}u_{ur2} \tag{19}$$

$$\frac{1}{2}u_{ul}^2+\mathrm{g}\eta_{ul}=\frac{1}{2}u_{ur1}^2+\mathrm{g}\eta_{ur1} \tag{20}$$

$$\frac{1}{2}u_{ul}^2+\mathrm{g}\eta_{ul}=\frac{1}{2}u_{ur2}^2+\mathrm{g}\eta_{ur2} \tag{21}$$

where η_{ui} and b_i are respectively the elevations and widths corresponding to the river cross-section areas A_i, with i=l, $r1$, $r2$. The non-linear system of six algebraic equations (16)-(21) is solved by means of the Newton-Raphson method. The fluxes at the interfaces are directly calculated from the characteristic variables.

It is worth realizing that a confluence point in the Mahakam River can become a bifurcation point (where water in a single channel is divided into two channels) due to the variations of the water discharge and tides. In that case, the numerical fluxes at the interfaces of the bifurcation point are computed using the computational procedure introduced above.

4 Model setup

4.1 Computational domain

The domain of interest in this study is limited to the region of tidal influence of the Mahakam river-lake-delta system (Fig. 1). This domain comprises 300 km of the Mahakam River and four tributaries, the three largest lakes (i.e. Lake Jempang, Lake Melingtang, and Lake Semayang) located about 150 km upstream of the delta, the Mahakam Delta, and the Makassar Strait. The four tributaries (i.e. Kedang Pahu, Belayan, Kedang Kepala, and Kedang Rantau) located in the middle part of the Mahakam River are included because they greatly contribute to the river flow. Also, among over thirty shallow-water lakes in the middle river catchment, the three largest lakes

mentioned above are taken into account in the computational domain since, again, these lakes act as a buffer of the river and regulate the water discharge in the lower part of the river. Finally, the multi-channel network in the delta is included in detail in the computational domain for taking into account several physical processes in the calculations.

4.2 Bathymetry

Data sets from various sources are available to represent the bathymetry of the studied system. The bathymetric data obtained from fieldwork campaigns with a single-beam echosounder during a period between 2008 and 2009 [27] are employed for the delta, the three lakes, and the river. The depth of the deltaic channels ranges from 5 to 15 m (see Fig. 3) while the water depth is of the order of 5 m in the three lakes. The water depth in the river varies greatly, and can reach up to 45 m in some meanders. In the Mahakam River and the four tributaries, the bathymetric data are used to interpolate river cross-sections. The global bathymetric GEBCO database (www.gebco.net) is used in the Makassar Strait and for the adjacent continental shelf.

4.3 Grid of the computational domain

The grid of the computational domain consists of a 2D sub-domain covering the three lakes, the whole delta, and the Makassar Strait and a 1D sub-domain representing the Mahakam River and four tributaries. The 2D sub-domain is discretized by means of an unstructured triangular grid whose resolution varies greatly in space while the river network within the 1D sub-domain has a resolution of about 100 m between cross-sections (Fig. 4). The 2D sub-domain allows for a very detailed representation of the delta. The resolution in the deltaic channels is such that there are at least two triangles (or elements) over the width of each tidal channel in the delta. The element (or mesh) size varies from 5 m in the narrowest branches of the delta to around 10 km in the deepest part of the Makassar Strait. The grid shown in Fig. 4 comprises 60,819 triangular elements and 3,700 line segments. This grid is generated using the open-source mesh generation software GMSH (www.geuz.org/gmsh, [28,29]).

The current unstructured grid allows for an accurate representation of the very complex

shorelines. The refinement criteria of the grid takes into account (i) the speed of the external gravity wave ($\sqrt{gh}$) [3,30,31] and (ii) the distance to the delta apex and coastlines in order to cluster grid nodes in regions where small scale processes are likely to take place.

It must be emphasized that in comparison with the computational grids used in previous studies [2,27,32] of the Mahakam Delta, the present computational grid is the first attemp to include most of the meandering and tidal branches as well as the creeks in the delta together with the main deltaic channels. The use of a model with such refinement of the computational grid is an important achievement because a wide range of temporal and spatial scales of several physical processes (e.g. tides, river flow) interacting with each other in the narrow and meandering tidal branches can be included in the calculations. For instance, Mandang and Yanagi [32] studied the dynamics of tide and tidal currents in the delta using a three-dimensional finite difference model, ECOMSED, with a structured grid that had a resolution of 200 meters. Such a horizontal grid resolution is unlikely to be suitable to represent the complex shorelines as well as the many small tidal channels existing in the delta. This is the reason why only the main deltaic channels are included in their study. An unstructured mesh comprising only the main deltaic channels is also used in the study of de Brye *et al*. [2], who quantified the division of water discharge through the main channels of the delta. Then, Sassi *et al*. [27] used exactly the same mesh to study the tidal impact on the division of water discharge at the delta apex (DAN and DAS) and first (FBN and FBS, in Fig. 4) bifurcations.

4.4 Boundary and initial conditions

As shown in Fig. 4, the downstream boundaries of the system are located at the entrance and the outlet of the Makassar Strait. The upstream boundaries are imposed at the city of Melak in the Mahakam River, where the tidal influence on the flow is negligible, and at the upstream end of the four tributaries (see Fig. 4b). The measured daily water discharge is imposed at the upstream boundary of the Mahakam River and the calculated daily water discharge from a rainfall-runoff model is prescribed at the upstream boundaries of the four tributaries. The tidal components (elevation and velocity harmonics) from the global ocean tidal model TPXO7.1 [33] are imposed at

the downstream boundaries. This global ocean tidal model allows for combining rationally both dynamic information from hydrodynamic equations and direct observation data from tide gauges and satellite altimetry [33]. In addition, this model also provides the best fits, in the least-squares sense, of the Laplace tidal equations and along-track averaged data from Topex/Poseidon and Jason satellites data [3,33].

Along the impermeable boundaries of coastlines, lakes, and the multi-channel network in the delta, the tangential stress is estimated using the following formulation:

$$\nu \frac{\partial u_t}{\partial n} = \alpha u_t \tag{22}$$

where α is the slip coefficient, $\partial u_t / \partial n$ is the normal derivative of the tangential velocity u_t. The constant coefficient α lies between zero and infinity, corresponding to free slip and no-slip conditions, respectively [34]. A finite value of α corresponds to a partial slip condition. In the current calculations, the adopted value $\alpha = 10^{-3}$ m/s [2] is applied, to allow for taking into account the effect of the transversal and tangential momentum flux along the impermeable boundaries.

The initial velocity in the computational domain is set equal to zero and an arbitrary value of 0.5 m is used for the initial water elevation, except in the lakes where a measured value of water elevation is imposed in the calibration step and a calculated value is used in the validation step. A spin up period of one neap-spring tidal cycle (about 15 days) is applied before the beginning of the period of interest. Regime conditions can be reached quickly after a few days and thus the effects of the initial conditions can be eliminated completely.

Calculations were performed using the high-performance computing facilities of the Université catholique de Louvain (www.uclouvain.be/cism). We used 24 processors in parallel for calculations and it takes about 1.5 days to simulate a period of 1 month using the refined computational grid shown in Fig. 4.

5 Calibration and validation results

5.1 Observations and simulation periods

In situ measurements including water elevation, flow velocity, and water discharge at various stations are available for estimating approximate values of the Manning coefficient in the system. Observations of water elevation at five stations (i.e. JWL, Pela Mahakam, Delta Apex, Delta North, Delta South, see Fig. 1) from May to August 2008 are used for calibration purposes (Section 5.3) while the long-term observations of water elevation (at Pela Mahakam, Muara Karman, Delta Apex, Delta North, and Delta South), flow velocity and water discharge (at Samarinda, DAN, DAS, FBN, and FBS) between October 2008 and June 2009 are employed for the validation of the model (Section 5.4). The water discharge at the upstream boundary in the Mahakam River varies between 1,200 and 2,300 m^3/s during the calibration period while it ranges from 870 to 2,800 m^3/s in the validation period.

5.2 Error estimates

Three different types of error, i.e. the root mean square (RMS) error, mean absolute error (MAE), and the Nash-Sutcliffe efficiency (NSE) are used to assess the quality of the simulations. The RMS error, MAE, and NSE are computed as follows:

$$\text{RMS error} = \sqrt{\frac{1}{N}\sum_{j=1}^{N}\left(X_{data,j} - X_{model,j}\right)^2} \tag{23}$$

$$\text{MAE} = \frac{1}{N}\sum_{j=1}^{N}\left|X_{data,j} - X_{model,j}\right| \tag{24}$$

$$\text{NSE} = 1 - \frac{\sum_{j=1}^{N}\left(X_{model,j} - X_{data,j}\right)^2}{\sum_{j=1}^{N}\left(X_{data,j} - X_{data,m}\right)^2} \tag{25}$$

where $X_{data,j}$ and $X_{model,j}$ are respectively the observations and model results of the quantity of interest, at the point number j in a time-series, $X_{data,m}$ is the mean value of observed quantity of interest, and N is the total number points in the considered time-series.

The RMS error is the most commonly used in practical applications. However, as shown in eq.

(23) for the RMS error, the differences between observed and computed values are calculated as square values (inside the square). Thus, the importance of larger values in time-series may be overestimated whereas lower values are neglected [35]. This is the reason why the MAE is additionally used. The RMS error and MAE are valuable indicators because they provide the error in the units of the quantity of interest, which is helpful in the analysis of the results. The NSE coefficient, that determines the relative magnitude of the residual variance (or noise) compared to the observations variance, is used to provide extensive information of comparisons.

The Pearson's correlation coefficient (r) is also applied for assessing the trend between computed results and observed data. The coefficient r is calculated as:

$$r = \frac{\sum_{j=1}^{N}\left(X_{data,j} - X_{data,m}\right)\left(X_{model,j} - X_{model,m}\right)}{\sqrt{\sum_{j=1}^{N}\left(X_{data,j} - X_{data,m}\right)^2}\sqrt{\sum_{j=1}^{N}\left(X_{model,j} - X_{model,m}\right)^2}}, \quad (26)$$

where $X_{model,m}$ is the mean value of computed results.

5.3 Calibration results

To calibrate the Manning coefficient, the computational domain of the Mahakam river-lake-delta system is provisionally divided into three regions, i.e. Mahakam River and tributaries, lakes, and delta and Makassar Strait. Different simulations are performed by using a constant Manning coefficient in each flow region. The Manning coefficient in the lakes changes from 0.023 s/m$^{1/3}$ to 0.045 s/m$^{1/3}$ while its value lies between 0.0175 s/m$^{1/3}$ and 0.0325 s/m$^{1/3}$ in the river and tributaries. In the remaining flow region, the Manning coefficient ranges from 0.019 s/m$^{1/3}$ to 0.035 s/m$^{1/3}$. Three values in each of the abovementioned ranges are selected for calibration purposes, resulting in twenty seven simulations (Table 1). According to the RMS errors of water elevation at five stations, the optimal value of the roughness coefficient is obtained in simulation a.14 (Table 1), with a value of 0.0275 s/m$^{1/3}$, 0.0305 s/m$^{1/3}$, and 0.023 s/m$^{1/3}$ for the river and tributaries, lakes, and delta and Makassar Strait, respectively. A slight improvement is obtained with an additional simulation where the Manning coefficient is taken as in simulation a.14 in the river and the lakes (i.e. 0.0275

and 0.0305), and then in the delta its value decreases linearly with the distance from the 1D / 2D connecting location (Fig. 4b) to the delta front, from 0.0275 $s/m^{1/3}$ to 0.023 $s/m^{1/3}$. Finally, the Manning coefficients corresponding to this additional simulation are considered as the optimal values. The computed water elevation obtained from this optimal distribution of the Manning coefficient is shown in Fig. 5 and Fig. 6 while the RMS error, MAE, NSE, and *r* coefficient at five stations are listed in Table 2.

Fig. 5 shows comparisons between observed and computed water elevations at JWL and Pela Mahakam stations. The model reproduces very well the observed water elevation at these stations. The RMS error of water elevation is only 6 cm at Pela Mahakam and 13 cm at JWL station during the comparable period. The MAE is less than 10 cm and the NSE coefficient is greater than 0.93, indicating that the model reproduces very well the observations. The correlation coefficient *r* is close to unity, revealing that both computed and observed water elevations show similar behaviors or variation trends during the calibration period.

In Lake Jempang, both simulations and observations show clearly that the tidal signal is of a marginal importance (Fig. 5a). These results suggest that the tide propagates up to a location located downstream of the lakes or around the Pela Mahakam. A discrepancy in the water elevation of about 20 cm occurs on 2008-06-16 at JWL station in the lake. This difference between observations and simulated water elevation can be explained by the lateral flow into the lake that is not taken into account in our simulations. At station Pela Mahakam, which is located closer to the delta, the tidal signal is felt more clearly than in the Lake Jempang (Fig. 5b). However, the fluctuation of the water elevation due to the tide at this station is still relatively small.

Fig. 6 shows the computed water elevation and the observations at Delta Apex, Delta South, and Delta North. A very good agreement between computed and observed water elevations is obtained at all three stations in the delta. The largest value of RMS errors at these stations is less than 13 cm in the two months period that is available for calibration. This error is only about 6.5% of the observed tidal range (i.e. about 2.0 m) at these stations. The MAE is more or less 5 cm while both

NSE and *r* coefficients are very close to unity.

An overestimation of low water elevation is observed at Delta Apex station. The use of approximate river discharges at the upstream tributaries, which are estimated from a rainfall-runoff model, could be the main reason for the error, as these estimates are less accurate for low flows. Another reason may be the use of a constant value of the bottom friction in the Mahakam River upstream of the station.

5.4 Validation results

Using the optimal values of the Manning coefficient obtained in the calibration step, a simulation for a 9 months period (from October 2008 to June 2009) is performed to validate the model and the parameters. The calculation errors and the detailed comparisons between computed results and observed data are presented for water elevation, flow velocity, and water discharge at various stations along the system under study.

5.4.1 Water elevation

As shown in Fig. 7a, the model reproduces very well the observed water elevation at Pela Mahakam station during the period from 2008-11-11 to 2008-11-19. The RMS error is only about 4 cm while the MAE is 3 cm (Table 3). The NSE and *r* coefficients are respectively 0.97 and 0.98 (Table 3), revealing that the model reproduces very well the observed values. These results suggest that appropriate values of the Manning coefficient were obtained for the upstream Mahakam River and tributaries and lakes.

In addition, there is only a minor tidal signal at Pela Mahakam station as shown in the calibration step. This result shows again that the tide propagates up to the Pela Mahakam location in the Mahakam River.

At Muara Karman station, which is located in the region downstream of the three tributaries (River Belayan, Kelang Kepala, and Kedang Rantau) and the lakes, the model reproduces rather well the observed water elevation (Fig. 7b). The RMS error, MAE, NSE, and *r* coefficient are equal to 10 cm, 7 cm, 0.89, and 0.95, respectively, for a two weeks period from 2008-11-04 to

2008-11-19. However, an overestimation and underestimation of the computed water elevation is observed at this station. Again, this difference can be explained by the inaccuracy of the water discharge imposed at the upstream boundaries in the tributaries.

As is the case for the calibration results, the model predicts very well the observed water elevation at three stations, namely Delta Apex, Delta South, and Delta North as shown in Fig. 8. The RMS error of water elevation is less than 12 cm at these stations. The MAE is about 9 cm while the NSE and *r* coefficients are about 0.95 (Table 3), indicating that the model correctly simulates the observed water elevation. However, an overestimation of the computed water elevation is observed in the low tidal situations.

5.4.2 Flow velocity

Fig. 9 illustrates the comparisons of the simulation results for the flow velocity and the measurement data in a long-term simulation period from 2009-02-20 to 2009-06-10 at Samarinda station. The model reproduces reasonably well the observed flow velocity in different neap-spring tidal cycles during the long-term simulation. The RMS error of flow velocity is 0.087 m/s, i.e. about 13% of the average value of the measured velocity while MAE of velocity is 0.07 m/s (Table 4). The *r* coefficient is 0.95 and the NSE coefficient is 0.89 (Table 4). These results show that the model successfully reproduces the flow velocity in the Mahakam River.

Fig. 10 shows the comparisons between computed and observed flow velocity at DAN, DAS, FBN, and FBS stations. The observed flow velocity in different spring and neap tides in the period from 2008-12-26 to 2009-01-05 are represented reasonably well by the model in general. As shown in Table 4, the RMS errors of flow velocity at DAN and DAS are 0.053 and 0.081 m/s, respectively. At FBN and FBS stations, these errors are 0.104 and 0.09 m/s (<20% of the average value of the measured velocity). A value of 0.042 and 0.063 m/s is obtained for the MAE at DAN and DAS, respectively, while the MAE respectively equals to 0.095 and 0.065 m/s at FBN and FBS. The NSE coefficient at all four stations is greater than 0.76 while the *r* coefficient is higher than 0.85.

At the low flow velocity situations (see Fig. 10), an overestimation of the calculated flow

velocity in the spring tides is obtained while an underestimation of the calculated velocity in the neap tides is achieved at DAS, FBN, and FBS stations. The difficulty in obtaining good reproduction of flow velocity at these stations is due to the complex flow around the bifurcations, which is highly variable, and probably also to the constant Manning coefficient in our simulations that does not represent well all the head-loss processes occurring around bifurcations.

5.4.3 Water discharge

The predicted and observed water discharges in a long-term simulation period from 2009-02-20 to 2009-06-10 at Samarinda station are shown in Fig. 11. The model reproduces reasonably well the observed water discharge in different neap-spring tidal cycles during the long-term simulation. The RMS error for the water discharge is 530 m^3/s (about 11% of the average value of the measured water discharge) while the value of MAE of water discharge is 420 m^3/s (Table 5). In addition, as for the flow velocity, the *r* coefficient is 0.95 and the NSE coefficient is 0.86 for water discharge. These results confirm again that the model successfully reproduces the flow in the Mahakam River.

The comparisons between computed and observed water discharges at four stations, namely DAN, DAS, FBN, and FBS are shown in Fig. 12. The results show that the simulations generally agree well with the observed water discharges measured in different spring and neap tides in the period from 2008-12-26 to 2009-01-05. The RMS errors of water discharge at DAN and DAS (Table 5) are 340 and 760 m^3/s, respectively and are equal to about 8% and 12% of the observed magnitude of water discharges at these stations. At FBN and FBS stations (Table 5), these errors are 17% (410 m^3/s) and 13% (720 m^3/s) of the measured water discharge. A value of 270 and 610 m^3/s is obtained for the MAE at DAN and DAS, respectively, while the MAE respectively equals to 370 and 540 m^3/s at FBN and FBS. The NSE coefficient at these stations is more or less 0.80 while the *r* coefficient is about 0.85 (Table 5).

Water discharges vary significantly in the northern and southern channel sections, depending on the tidal conditions. Due to wider channel sections in the southern channels, a larger amount of water discharges into the southern channels (DAS and FBS) in comparison with the northern

channels (DAN and FBN). As shown in Fig. 12b and Fig. 12d for the channel sections in the southern channels, the model predicts very well the observations at large discharges. At low discharges (corresponding to high water situations), the model overestimates the water discharge observations at the high water of spring tide on 2008-12-26 at DAS and on 2008-12-27 at FBS. The computed water discharge underestimates the observations at the high water of neap tide on 2009-01-04 at DAS and on 2009-01-03 at FBS. These discrepancies may be due to the use of a constant value of the Manning coefficient and the inability of the model to take into account lateral secondary circulation flows caused by local channel curvature. A vertical wall is assumed at impermeable coastlines. This assumption may result in inaccuracy of the wetted channel section area corresponding to high waters in calculations and, hence, can be another reason for the discrepancies in the water discharge.

6 Discussion

6.1 Water division at bifurcations in the delta

The delta presents many bifurcations (Fig. 1) that can affect the division of water discharge in the downstream channels. Fig. 13 shows the variation in water discharge division over the downstream channels of the delta apex (DAN and DAS) and first (FBN and FBS) bifurcations at different tidal conditions, e.g. neap or spring tide. The model represents very well the observed division of water discharge at both bifurcations, with an improvement compared to the numerical simulations reported by Sassi *et al.* [27], in which (i) the water discharge division over the downstream channels is only biased towards the northern channels, (ii) the simulated water discharge division at delta apex bifurcation during spring tide is too asymmetrical, and (iii) the simulations of the water discharge division lead to values smaller than those measured *in situ*. This improvement may be due to the use, in the present study, of different values of the Manning coefficient in the upstream region of the delta and in the delta itselt.

Fig. 14 shows the specific water discharge ($q = Q / b$) at different cross-sections in the northern and southern channels downstream of the delta apex and first bifurcations in the delta (Fig. 4b).

Both computed results and observations show that the specific water discharge is directed towards the northern channel at the delta apex bifurcation (Fig. 14a). This trend in specific water discharge division may result from the differences in local flow, e.g. tidal motion in northern and southern branch channels.

Results for the first bifurcation (FBN and FBS) are shown in Fig. 14b. For low discharges, a similar trend as in Fig. 14a is observed, i.e. the specific water discharge is directed towards the northern channel. However, for high discharges (corresponding to low tides), the specific water discharge is generally directed towards the southern channel (FBS), presenting an opposite trend in comparison with the delta apex bifurcation. There is a local depositional area (sand bar) in the middle channel downstream of DAS (Fig. 4b) that extends over few kilometers before the first bifurcation. Due to this sand bar, the water flow is divided into two parts, with the dominant water directed towards the northern channel (FBN). This is the reason why the specific water discharge is directed towards the northern branch at low discharges. At high flow discharges, an opposite trend of specific water discharge is obtained. Indeed, the effects of the sand bar become negligible, as for higher water levels the channel in the southern branch is much deeper and wider than the northern branch.

6.2 Effects of the lakes

In order to investigate the influence of the three largest lakes, one simulation including these lakes and one simulation excluding these lakes are performed for a low flow period from June to November 2009. The optimal values of the Manning coefficient in Section 5 are used in both simulations. The computational grid shown in Fig. 4 is also used, with the particular grid of the three lakes being removed for the later simulation. Fig. 15 shows the computed water elevation from these simulations at three stations, namely Pela Mahakam, Muara Karman, and Samarinda (see Fig. 1). The discrepancy in the water elevation with and without including the lakes is about 35 cm (i.e. 28% of the water elevation magnitude that is obtained in the case without the lakes) at Pela Mahakam, 25 cm (i.e. 18% of the water elevation magnitude) at Muara Karman, and 10 cm (i.e. 6%

of the water elevation magnitude) at Samarinda station, revealing that the influence of the lakes on the water elevation in the Mahakam River decreases in the downstream direction as expected. At Delta Apex, Delta North, and Delta South stations, this difference (not shown) is less than 5 cm. These results suggest that the effect of the lakes is not negligible and, hence, is worth investigating in detail. This will be done in the next stage of the research.

The computed water discharges at Pela Mahakam, Muara Karman, and Samarinda when including and excluding the lakes into the computational domain are shown in Fig. 16. If the three lakes are added in the computational domain, the magnitude of water discharge will be increased by 340 m^3/s (i.e. 11% of the mean annual river discharge of the Mahakam River), 400 m^3/s (i.e. 13% of the mean annual river discharge of the Mahakam River), and 500 m^3/s (i.e. 17% of the mean annual river discharge of the Mahakam River) at the Pela Mahakam, Muara Karman, and Samarinda station, respectively, for situations of water flowing in seaward direction. Conversely, when water flows in the direction from the sea to the river corresponding to the negative water discharge in Fig. 16, a water discharge of about 800 m^3/s (i.e. 27% of the mean annual river discharge of the Mahakam River) will flow in these three lakes, as shown in Fig. 16a. These results suggest that the model is able to reproduce the interconnection between the lakes and the river.

6.3 Effects of the computational grid

To investigate the effects of grid resolution on the computed results, a simulation on a coarser grid (denoted by mesh A) and a simulation on a finer grid (denoted by mesh C) are also performed. The total numbers of triangular elements in the 2D sub-domain is 49,175 for mesh A and 80,222 for mesh C and both meshes have 3,700 line segments in the 1D sub-domain. The procedure for generating mesh A and mesh C is exactly the same as those using for creating the computational grid shown in Fig. 4 (denoted by mesh B). The boundary conditions and the optimal values of the Manning coefficient (n = 0.0275 $s/m^{1/3}$ in the river and tributaries, n = 0.0305 $s/m^{1/3}$ in the three lakes, n = 0.023 $s/m^{1/3}$ in the Makassar Strait, and n = 0.023-0.0275 $s/m^{1/3}$ in the delta) presented in the previous section are used in both additional simulations. The statistical evaluation of the

549 different type of errors when using mesh A and mesh C is summarized in Table 6 while, again,
550 these errors when using mesh B are listed in Table 2. It can be observed that slight differences are
551 observed when using different meshes, but the overall statistical evaluation of the different type of
552 errors at all five water elevation stations appears to be similar when using different meshes. This is
553 because the resolution of each computational grid is still defined by physical processes, i.e. the local
554 mesh size is defined to be proportional to the square root of the bathymetry and the refinement of
555 each grid also still depends on the distance to the delta apex and coastlines.

556 **6.4 Reasons for the discrepancies and future work**

557 A constant value of the bottom friction was assumed for the tributaries and along the Mahakam
558 River, in order to render the calibration as simple as possible. The use of such constant values may
559 not be suitable when considering the roughness coefficient of the tributaries and the river in reality.
560 In addition, the effects of secondary flows can be significant in the meandering channels of the delta
561 as well as in the Mahakam River itself [36]. These secondary flows are not taken into account in the
562 calculations, which could explain some of the differences between simulations and observations at
563 some stations. Moreover, the uncertainty in the determination of the water discharge at the upstream
564 boundaries of the tributaries in the model, caused by using a rainfall-runoff model, can be another
565 reason for the observed discrepancy. Furthermore, the absence of baroclinic effects, which cannot
566 be taken into account in the present depth- and section-averaged model, may be an additional reason
567 for the discrepancy between observations and simulations. Finally, regarding the comparisons
568 between computed and observed flow velocity as well as water discharges at four channel sections
569 located downstream of the delta apex and first bifurcations, the difference between them can be
570 explained by several factors, e.g. a bend upstream of bifurcations, the width-depth ratio of the
571 upstream channel, local bank irregularities, differences of roughness [37].

572 In each flow region such as Mahakam River and tributaries or lakes, variation of the Manning
573 coefficient corresponding to the change of the local water depth was not considered in this study.
574 Previous studies [38,39] suggested that the Manning coefficient can be changed with the variation

of the water depth. Regarding the Mahakam River, the water depth can vary considerably, depending on the location. Further investigation of the Manning coefficient as a function of the local water depth will be considered in the future modelling effort for exploring the spatial variation of the Manning coefficient in each region of the studied system.

Previous study [12] on flooding in the middle Mahakam River catchment shows that bank overtopping can occur during a flood situation in floodplain regions located around the Melintang Lake. During flood periods, these regions are flooded and water flows through these regions to the lake. In the connecting channels between the lakes and the Mahakam River, flow overtopping can also happen in flood situations. Due to the effects of flow overtopping, the channel banks can be eroded, resulting in an increase of the channel width. However, in the framework of the present numerical model, the increase of channel width caused by flow overtopping has not been considered yet and a vertical wall is assumed to be used in such situations, preventing the inundation of the floodplain. Treatments of overtopping flow and simulations in a long-term period of several years are foreseen in the future to further quantify the balance of water inputs to and outputs from the lakes.

7 Summary and conclusion

The Mahakam river-lake-delta system presents a continuous riverine and marine environment including various interconnected regions, i.e. a river and its tributaries, lakes, a delta, and the adjacent coastal ocean, with complicated processes of the flow. In this study, the unstructured-mesh, finite element model SLIM was applied to this river-lake-delta system, using a coupled 1D / 2D version of the model, (i) to allow for reproducing the flow from the upstream to the open sea and (ii) to have better understanding of the flow processes occurring at different temporal and spatial scales in the system. The complex geometry, especially in the deltaic region, was represented in detail in the computational domain in order to take into account several physical processes in the calculations.

The appropriate values of the Manning coefficient in each part of the system, i.e. Mahakam

River and tributaries, lakes, delta, and Makassar Strait were calibrated. The model was then validated to confirm the appropriate values of the Manning coefficient. A good agreement was achieved between the computed results and observations for the water elevation at six stations, and for the velocity and water discharge at the other five stations. The RMS error and MAE were only about 10 cm at all water elevation stations while the maximum value of these errors for water discharge was of the order of 12% of the observed values. The RMS error and MAE of velocity were smaller than 20% of the observed velocity. The NSE coefficient was 0.95 at six water elevation stations and its value was about 0.80 at the stations of velocity and water discharge. The Pearson's correlation coefficient between computed results and field data was very close to unity at all stations. The coupled 1D / 2D model of the unstructured-mesh, finite element model SLIM successfully reproduced the observations of the flow in the Mahakam river-lake-delta system.

Using the computations, firstly, in terms of division of water at the bifurcations, the model reproduced reasonably well the observations at the delta apex and at the first bifurcations in the delta. Secondly, the effects of three lakes on the flow in the lower part of the Mahakam River were also quantified, showing that these lakes contribute about 20% of the mean annual river discharge of the Mahakam River in the considered low flow period. Thirdly, the region of the lakes, which is located about 150 km upstream of the Mahakam Delta, was found as the limit of the tidal propagation in the Mahakam river-lake-delta system. Finally, the grid resolution was preliminarily explored, revealing that the overall evaluation of the errors at five water elevation stations appears to be similar when using three different meshes, because the resolution of each mesh is still defined by the same physical processes.

The results obtained in the present study are believed to be useful for studying transport processes of various constituents (e.g. sediment, salinity) in the system as well as water renewal timescales in the deltaic regions in the future. In addition, the coupled 1D / 2D model of the unstructured-mesh, finite element model SLIM uses a computational grid that allows for an accurate representation of complex topographies and an increase in spatial resolution in areas of interest,

627 which makes the model to be very suitable and computationally efficient for simulating the flow in
628 other river-lake-delta systems like the one associated with the Mahakam River. Fine mesh can be
629 used in the domain of interest instead of in the whole computational domain, and thus, this can
630 reduce the computational time due to a decrease of the number of elements. Moreover, different
631 spatial scales of the flow processes from the river to the coastal ocean and deep margin can be also
632 simulated.

633 ## Acknowledgements

634 This study was conducted under the auspices of the project "Taking up the challenges of multi-scale
635 marine modelling" which is funded by the Communauté Française de Belgique under contract ARC
636 10/15-028 (Actions de Recherche Concertées) with the aim of developing and using SLIM.
637 Computational resources have been provided by the high-performance computing facilities of the
638 Université catholique de Louvain (CISM/UCL) and the Consortium des Equipements de Calcul
639 Intensif en Fédération Wallonie Bruxelles (CECI) funded by the Fonds de la Recherche Scientifique
640 de Belgique (F.R.S.-FNRS). Eric Deleersnijder and Sandra Soares-Frazão are honorary research
641 associates with this institution.

References

1. Peters DL, Buttle JM (2010) The effects of flow regulation and climatic variability on obstructed drainage and reverse flow contribution in a Northern river–lake–Delta complex, Mackenzie basin headwaters River Research and Applications 26:1065-1089.
2. de Brye B, Schellen S, Sassi M, Vermeulen B, Karna T, Deleersijder E, Hoitink T (2011) Preliminary results of a finite-element, multi-scale model of the Mahakam Delta (Indonesia). Ocean Dynamics 61:1107-1120.
3. de Brye B, de Brauwere A, Gourgue O, Kärnä T, Lambrechts J, Comblen R, Deleersnijder E (2010) A finite-element, multi-scale model of the Scheldt tributaries, river, estuary and ROFI. Coastal Engineering 57:850-863.
4. Wu W, Li Y (1992) One- and two-dimensional nesting mathematical model for river flow and

sedimentation; Karlsruhe, Germany. p 547-554.

5. Zhang SQ (1999) One-D and two-D combined model for estuary sedimentation. International Journal of Sediment Research 14(1):37-45.

6. Martini P, Carniello L, Avanzi C (2004) Two dimensional modelling of flood flows and suspended sediment transport: the case of Brenta river, Veneto (Italy). Natural Hazards and Earth System Sciences 4:165-181.

7. Cook A, Merwade V (2009) Effect of topographic data, geometric configuration and modeling approach on flood inundation mapping. Journal of Hydrology 377:131-142.

8. Pietrzak J, Deleersnijder E, Schröter J (2005) Special Issue: The second International workshop on unstructured mesh numerical modelling of coastal, shelf and ocean flows Delft, The Netherlands, September 23-25, 2003. Ocean Modelling 10(1-2):1-3.

9. Deleersnijder E, Legat V, Lermusiaux PFJ (2010) Multi-scale modeling of coastal, shelf and global ocean dynamic. Ocean Dynamics 60:1357-1359.

10. Lambrechts J, Hanert E, Deleersnijder E, Bernard P-E, Legat V, Remacle J-F, Wolanski E (2008b) A multi-scale model of the hydrodynamics of the whole Great Barrier Reef. Estuarine, Coastal and Shelf Science 79:143-151.

11. Allen GP, Chambers JLC (1998) Sedimentation in the modern and Miocene Mahakam delta; Jakarta. p 236.

12. Hidayat H, Hoekman DH, Vissers MAM, Hoitink AJF (2012) Flood occurrence mapping of the middle Mahakam lowland area using satellite radar. Hydrology and Earth System Sciences 16:1805-1816.

13. Roberts HH, Sydow J (2003) Later quaternary stratigraphy and sedimentology of the offshore Mahakam delta, East Kalimantan (Indonesia). Tropical Deltas of Southeast Asia: Sedimentology, Stratigraphy, and Petroleum Geology 76:125-145.

14. Storms JEA, Hoogendoorn RM, Dam RAC, Hoitink AJF, Koonenberg SB (2005) Late-Holocene evolution of the Mahakam delta, East Kalimantan, Indonesia. Sedimentary

Geology 180:149-166.

15. Hall R, Cloke IR, Nur'aini S (2009) The North Makassar Straits: what lies beneath? Petroleum Geoscience 15:147-158.

16. Susanto RD, Ffield A, Gordon AL, Adi TR (2012) Variability of Indonesian throughflow within Makassar Strait, 2004-2009. Journal of Geophysical Research 117, C09013, doi:10.1029/2012JC008096.

17. Adcroft A, Marshall D (1998) How slippery are piecewise-constant coastlines in numerical ocean models? . Tellus 50A(1):95-108.

18. Edmonds DA, Slingerland RL (2010) Significant effect of sediment cohesive on delta morphology. Nature Geoscience 3:105-109.

19. Budhiman S, Salama SM, Vekerdy Z, Verhoef W (2012) Deriving optical properties of Mahakam Delta coastal waters, Indonesia using *in situ* measurements and ocean color model inversion. ISPRS Journal of Photogrammetry and Remote Sensing 68:157-169.

20. Budiyanto F, Lestari (2013) Study of metal contaminant level in the Mahakam Delta: Sediment and dissolved metal perpectives. Journal of Coastal Development 16(2):147-157.

21. Salahuddin, Lambiase JJ (2013) Sediment dynamics and depositional systems of the Mahakam Delta, Indonesia: ongoing delta abandonment on a tide-dominated coast. Journal of Sedimentary Research 83:503-521.

22. Smagorinsky J (1963) General circulation experiments with the primitive equations. Monthly Weather Review 91:99-164.

23. Darby SE, Thorne CR (1996) Predicting stage-discharge curves in channels with bank vegetation. Journal of Hydraulic Engineering 122(10):583-586.

24. Kärnä T, de Brye B, Gourgue O, Lambrechts J, Comblen R, Legat V, Deleersnijder E (2011) A fully implicit wetting-drying method for DG-FEM shallow water models, with an application to the Scheldt Estuary. Computer Methods in Applied Mechanics and Engineering 200:509-524.

25. Comblen R, Lambrechts J, Remacle J-F, Legat V (2010) Practical evaluation of five partly discontinuous finite element pairs for the non-conservative shallow water equations. International Journal for Numerical Methods in Fluids 63:701-724.

26. Sherwin S, Formaggia L, Peiro J (2003) Computational modelling of 1D blood flow with variable mechanical properties and its applications to the simulation of wave propagation in the human arterial system. Journal for Numerical Methods in Fluids 43:673-700.

27. Sassi M, Hoitink AJF, de Brye B, Vermeulen B, Deleersnijder E (2011) Tidal impact on the division of river discharge over distributary channels in the Mahakam Delta. Ocean Dynamics 61:2211-2228.

28. Lambrechts J, Comblen R, Legat V, Geuzaine C, Remacle J-F (2008a) Multiscale mesh generation on the phere. Ocean Dynamics 58:461-473.

29. Geuzaine C, Remacle J-F (2009) GMSH: a finite element mesh generator with built-in pre-and post-processing facilities. International Journal for Numerical Method in Engineering 79(11):1309-1331.

30. Legrand S, Deleersnijder E, Hanert E, Legat V, Wolanski E (2006) High-resolution unstructured meshes for hydrodynamic models of the Great Barrier Reef, Australia. Estuarine, Coastal and Shelf Science 68:36-46.

31. Legrand S, Deleersnijder E, Delhez EJM, Legat V (2007) Unstructured anisotropic mesh generation for the Northwestern European continental shelf, the continental slope and the neighbouring ocean. Continental Shelf Research 27:1344-1356.

32. Mandang I, Yanagi T (2008) Tide and tidal current in the Mahakam Estuary, East Kalimantan, Indonesia. Coastal Marine Science 32(1):1-8.

33. Egbert GD, Bennet AF, Foreman MGG (1994) TOPEX/POSEIDON tides estimated using a global inverse model. Journal of Geophysical Research 99(C12):24821-24852.

34. Haidvogel DB, McWilliams JC, Gent PR (1991) Boundary current separation in a quasigeostrophic, eddy-resolving ocean circulation model. Journal of Physical Oceanography

22:882-902.

35. Legates DR, McCabe JGJ (1999) Evaluating the use of "goodness-of-fit" measures in hydrologic and hydroclimatic model validation. Water Resources Research 35(1):233-241.

36. Sassi M, Hoitink AJF, Vermeulen B, Hidayat H (2013) Sediment discharge division at two tidally influenced river bifurcations. Water Resources Research 49(4):2119-2134.

37. Kleinhans MG, Jagers HRA, Mosselman E, Sloff CJ (2008) Bifurcation dynamics and avulsion duration in meandering rivers by one-dimensional and three-dimensional models. Water Resources Research 44,W08454:doi:10.1029/2007WR005912.

38. Shih SF, Rahi GS (1982) Seasonal variation of Manning's roughness coefficient in a subtropical marsh. Transaction of the ASAF 25(1):116-119.

39. Bao W-M, Zhang Z-Q, Qu S-M (2009) Dynamic Correction of Roughness in the Hydrodynamic Model. Journal of Hydrodynamics 21(2):255-263.

40. Toro, E. (1997). Riemann Solvers and Numerical Methods for Fluid Dynamics, a Practical Introduction. Springer, Berlin.

Tables

Table 1 RMS error of water elevation at five measurement stations for the calibration phase

Simulation	Manning coefficient			RMS error of water elevation (cm)				
	lakes	river and tributaries	delta and Makassar Strait	JWL	Pela Mahakam	Delta North	Delta South	Delta Apex
a.01			0.019	28.1	20.5	8.4	7.6	14.6
a.02		0.0175	0.023	27.3	19.3	8.3	7.4	15.1
a.03			0.035	24.8	16.2	8.8	8.1	23.6
a.04			0.019	13.5	6.0	8.4	7.6	15.2
a.05	0.023	0.0275	0.023	13.2	5.7	8.3	7.4	13.9
a.06			0.035	12.6	5.3	8.8	8.1	21.5
a.07			0.019	14.1	8.5	8.4	7.6	16.2
a.08		0.0325	0.023	14.2	8.9	8.3	7.4	13.9
a.09			0.035	14.8	10.2	8.8	8.1	20.3
a.10			0.019	28.1	20.6	8.4	7.6	14.6
a.11		0.0175	0.023	27.2	19.4	8.3	7.4	15.1
a.12			0.035	24.7	16.3	8.8	8.1	23.6
a.13			0.019	13.5	6.0	8.4	7.6	15.2
a.14	0.0305	0.0275	0.023	***13.2***	***5.7***	***8.3***	***7.4***	***12.8***
a.15			0.035	13.7	5.9	9.2	8.3	21.4
a.16			0.019	14.1	8.5	8.4	7.6	16.2
a.17		0.0325	0.023	14.3	8.9	8.3	7.4	13.9
a.18			0.035	14.8	10.1	8.8	8.1	20.3
a.19			0.019	27.9	20.9	8.5	7.7	14.7
a.20		0.0175	0.023	27.1	19.7	8.3	7.4	15.2
a.21			0.035	24.6	16.4	8.8	8.1	23.6
a.22			0.019	13.5	6.1	8.4	7.6	15.2
a.23	0.045	0.0275	0.023	13.3	5.8	8.3	7.4	12.9
a.24			0.035	12.7	5.4	8.8	8.1	21.5
a.25			0.019	14.2	8.5	8.4	7.6	16.2
a.26		0.0325	0.023	14.4	8.8	8.3	7.4	13.9
a.27			0.035	15.0	10.1	8.8	8.1	20.3

Table 2 RMS error, MAE, NSE, and r at water elevation stations for the calibration phase

Station	Water elevation			
	RMS error (cm)	MAE (cm)	NSE	*r*
JWL	13.1	10.4	0.93	0.96
Pela Mahakam	5.6	4.6	0.96	0.98
Delta North	8.3	6.7	0.98	0.99
Delta South	7.4	6.0	0.98	0.99
Delta Apex	10.2	8.0	0.93	0.97

Table 3 RMS error, MAE, NSE, and r at water elevation stations for the validation phase

Station	Water elevation			
	RMS error (cm)	MAE (cm)	NSE	*r*
Pela Mahakam	3.9	3.3	0.97	0.98
Muara Karman	10	7.1	0.89	0.95
Delta North	10.9	8.8	0.96	0.98
Delta South	10.4	8.4	0.96	0.98
Delta Apex	11.7	9.3	0.92	0.96

Table 4 RMS error, MAE, NSE, and r at flow velocity stations for the validation phase

Station	Flow velocity			
	RMS error (m/s)	MAE (m/s)	NSE	*r*
Samarinda	0.087	0.069	0.89	0.95
DAN	0.053	0.042	0.88	0.94
DAS	0.081	0.063	0.79	0.85
FBN	0.104	0.095	0.76	0.90
FBS	0.090	0.065	0.77	0.88

Table 5 RMS error, MAE, NSE, and r at water discharge stations for the validation phase

Station	Water discharge			
	RMS error (m^3/s)	MAE (m^3/s)	NSE	*r*
Samarinda	530	420	0.86	0.95
DAN	340	270	0.85	0.92
DAS	760	610	0.71	0.83
FBN	410	370	0.75	0.87
FBS	720	540	0.79	0.89

Table 6 Statistical evaluation of the different type of errors at water elevation stations when using different meshes

Mesh / Station	Mesh A				Mesh C			
	RMS error	MAE	NSE	*r*	RMS error	MAE	NSE	*r*
JWL	13.2	10.7	0.93	0.97	12.7	10.5	0.93	0.97
Pela Mahakam	5.6	4.7	0.96	0.98	5.6	4.7	0.96	0.98
Delta North	8.2	6.7	0.98	0.99	8.0	6.6	0.98	0.99
Delta South	7.4	6.0	0.98	0.99	7.3	5.8	0.98	0.99
Delta Apex	10.3	8.3	0.93	0.97	9.8	8.0	0.93	0.97

Figures

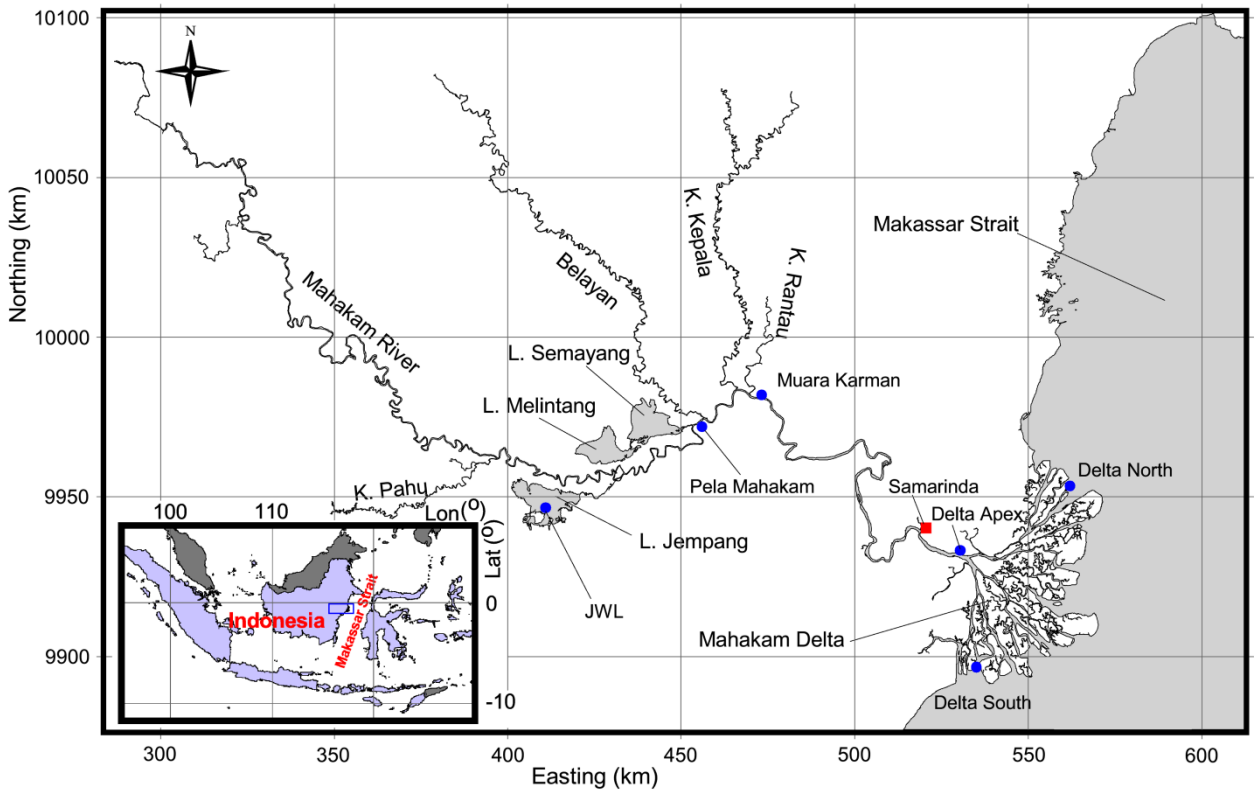

Fig. 1 Map of the tropical Mahakam river-lake-delta system, Indonesia: *blue dots* indicate the water elevation stations while *red square* denotes the flow velocity and water discharge station.

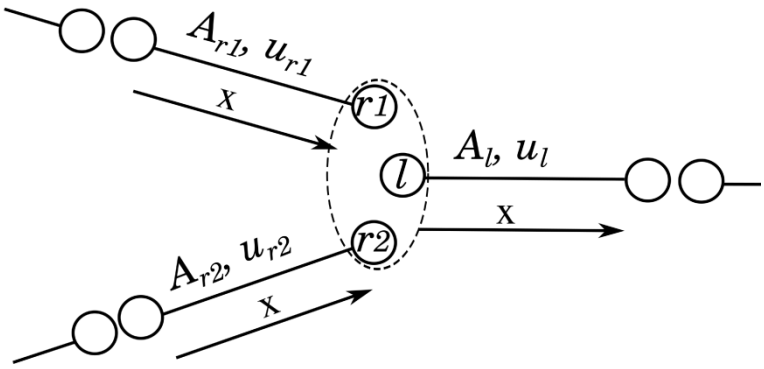

Fig. 2: Schematic diagram of line segments and nodes at a confluence point, where the space coordinate *x* increases in the flow direction.

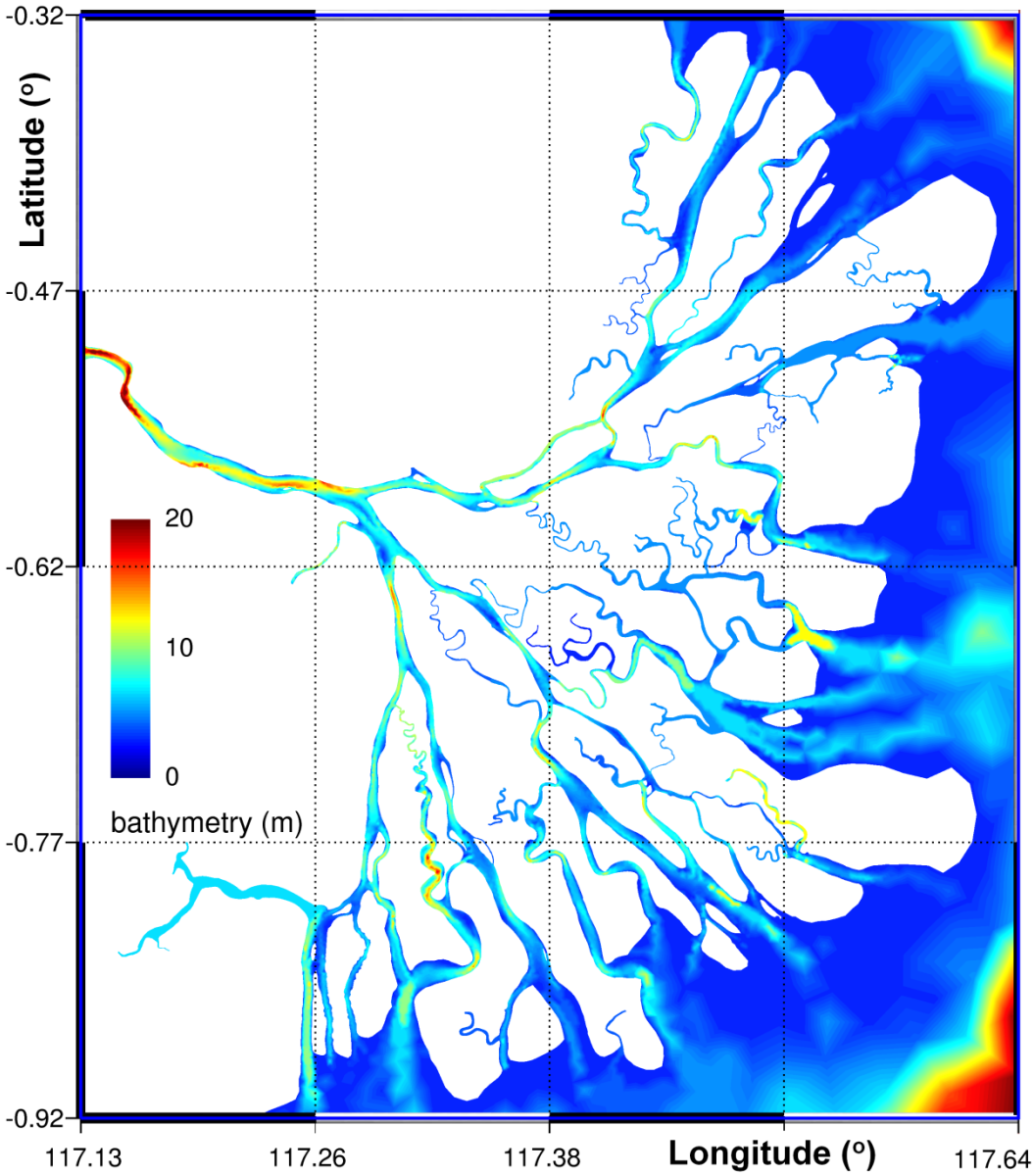

Fig. 3: Bathymetry in the Mahakam Delta.

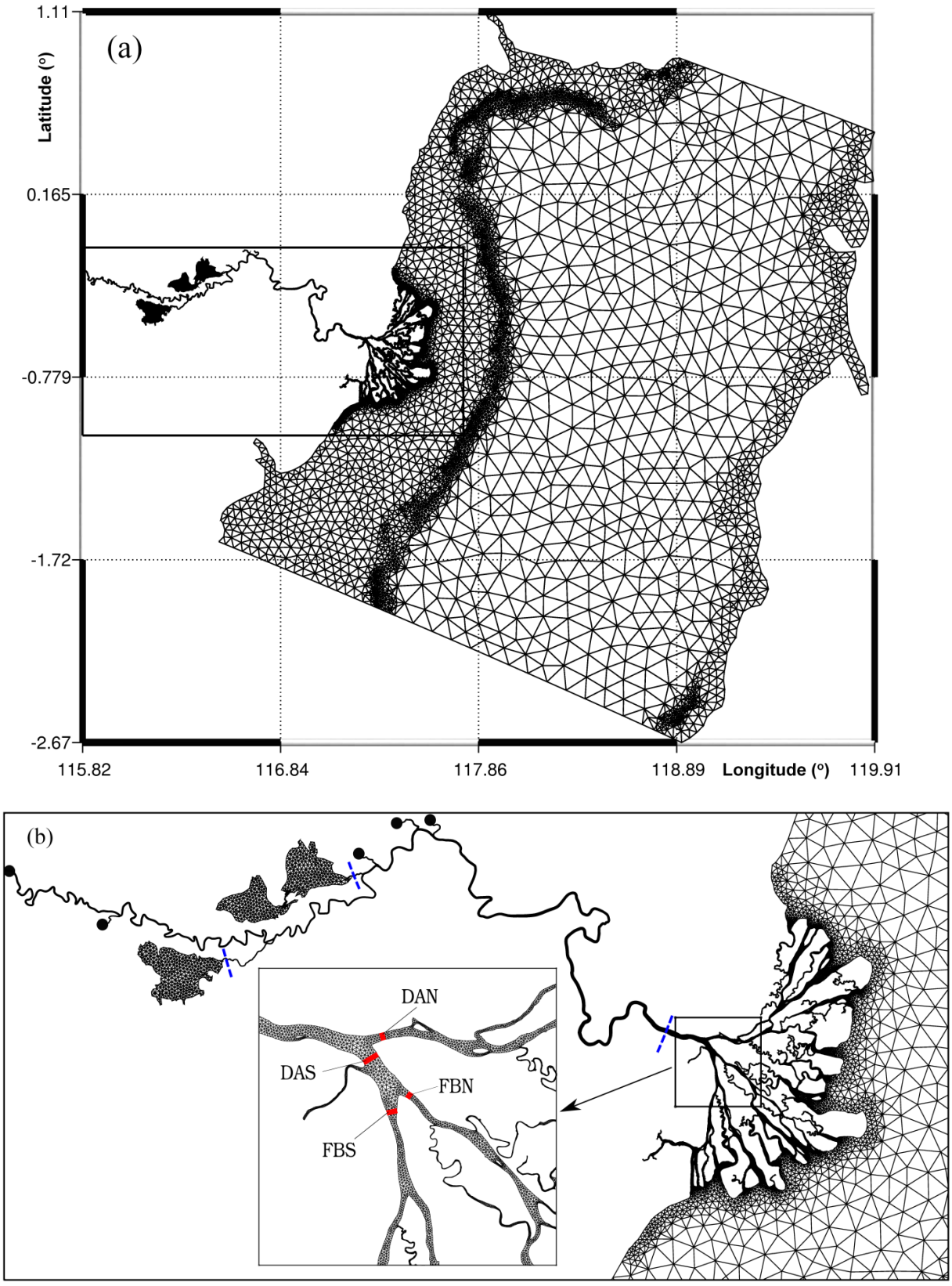

Fig. 4 Computational grid of the Mahakam river-lake-delta system: (a) mesh of the whole computational domain, with 60,819 triangles and 3,700 line segments and (b) zoom on the delta and upstream part of the computational domain: *blue dash-lines* indicate the interfaces between the 1D and 2D grids, *black dots* denote upstream boundaries locations, and *red squares* represent the flow velocity and water discharge stations.

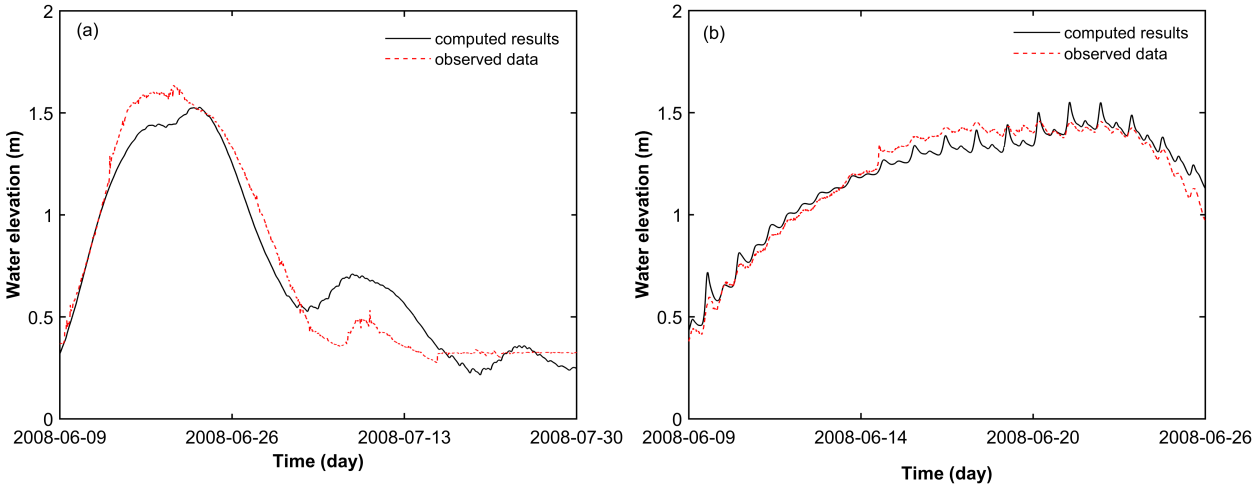

Fig. 5 Observed and computed water elevation at: (a) JWL and (b) Pela Mahakam stations (Fig. 1) during the calibration period.

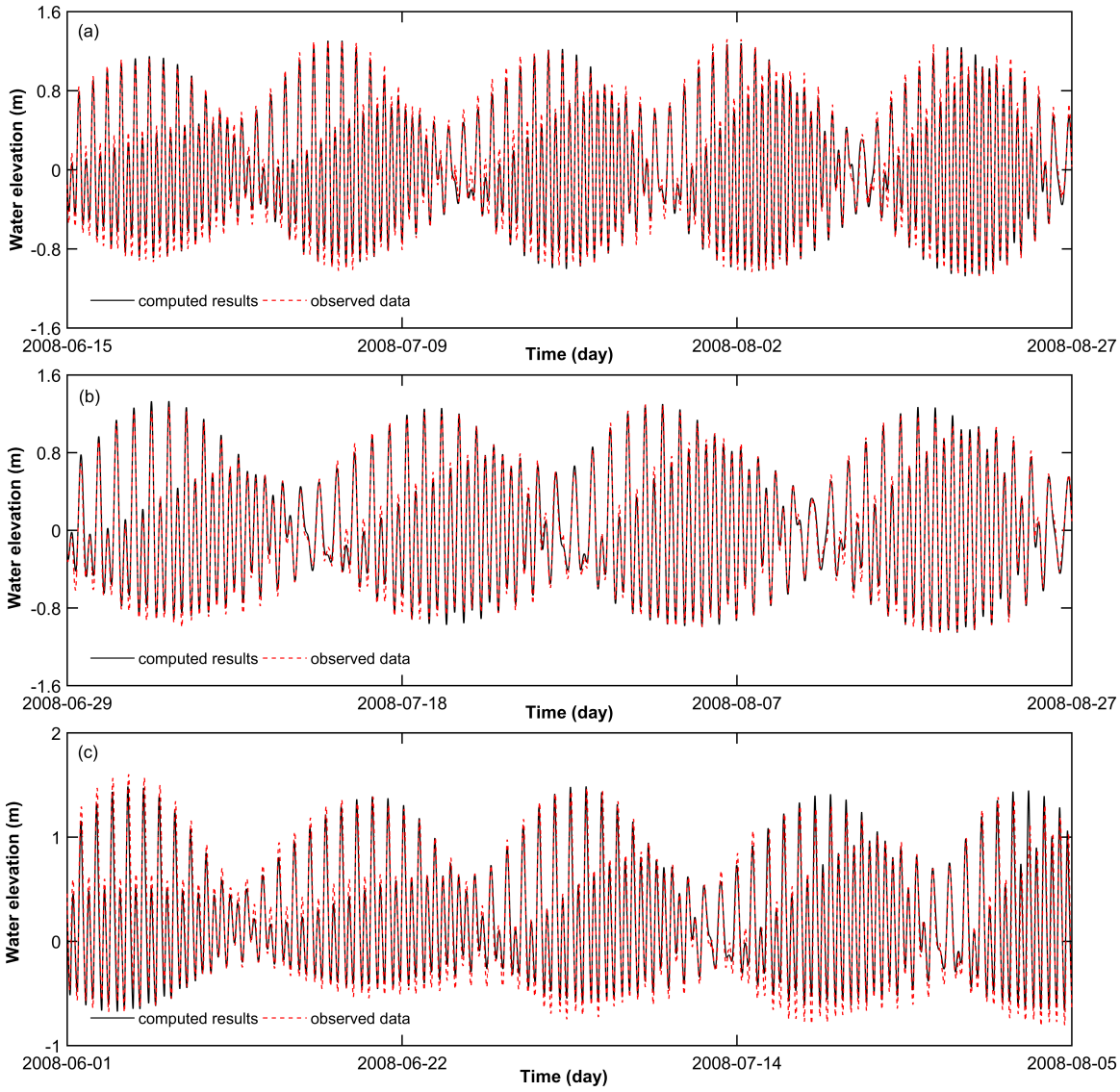

Fig. 6 Observed and computed water elevation at: (a) Delta North, (b) Delta South, and (c) Delta Apex stations (Fig. 1) during the calibration period.

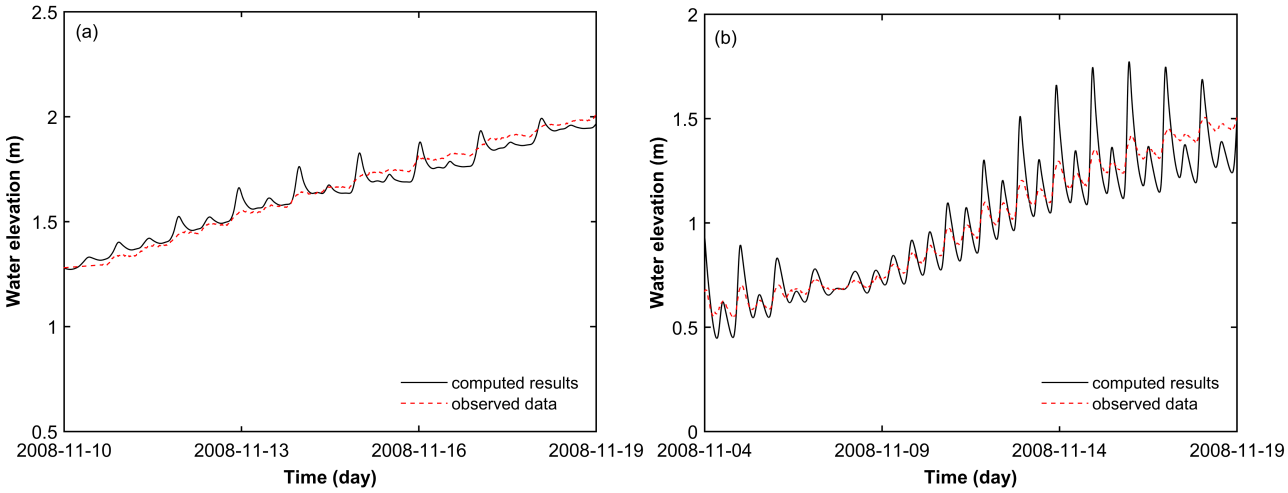

Fig. 7 Observed and computed water elevation at: (a) Pela Mahakam and (b) Muara Karman stations (Fig. 1) during the validation period.

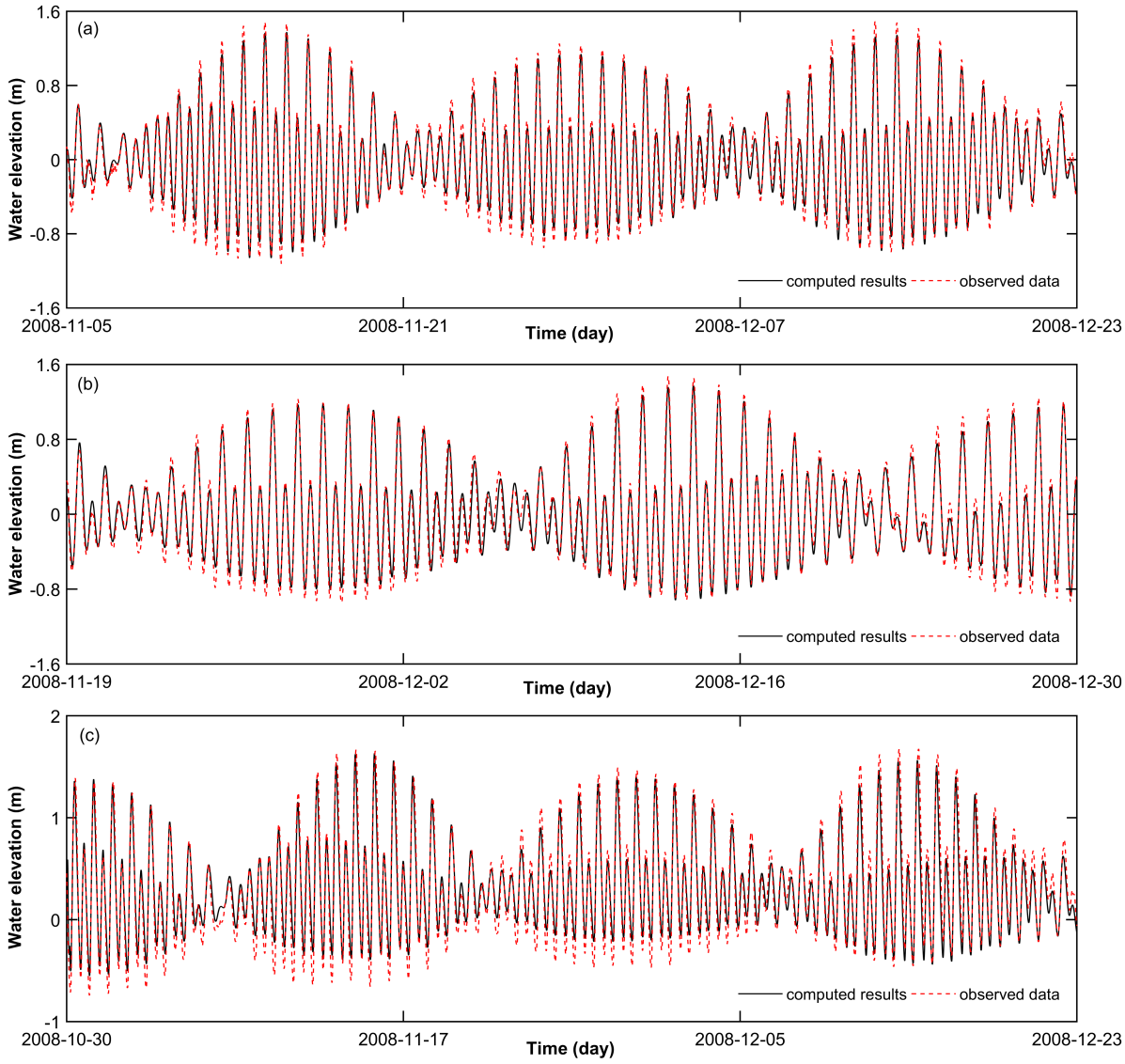

Fig. 8 Observed and computed water elevation at: (a) Delta North, (b) Delta South, and (c) Delta Apex stations (Fig. 1) during the validation period.

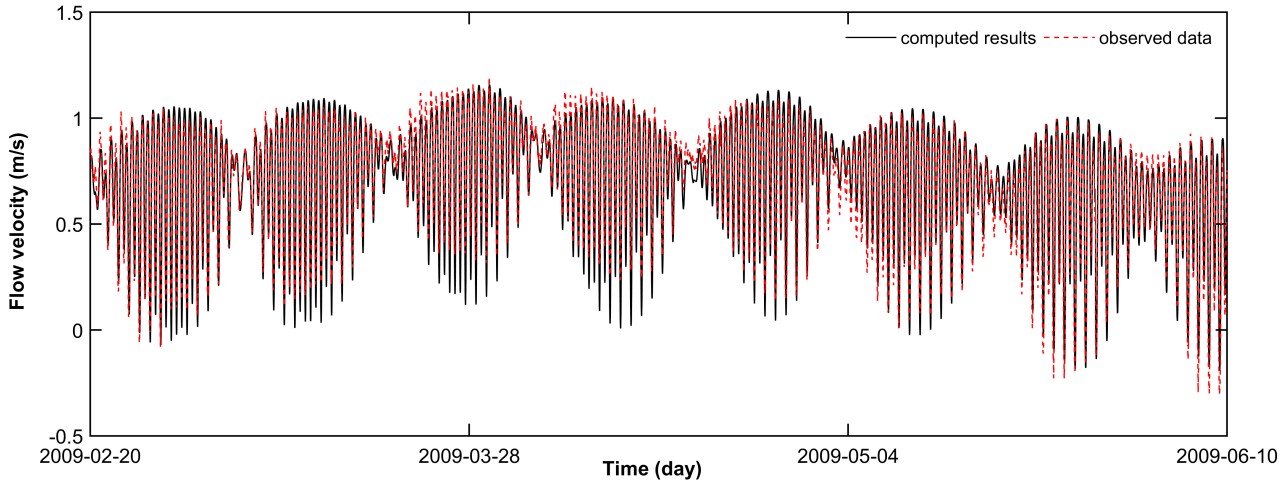

Fig. 9 Observed data and computed results of flow velocity at Samarinda station, where positive velocity coincides with seaward direction.

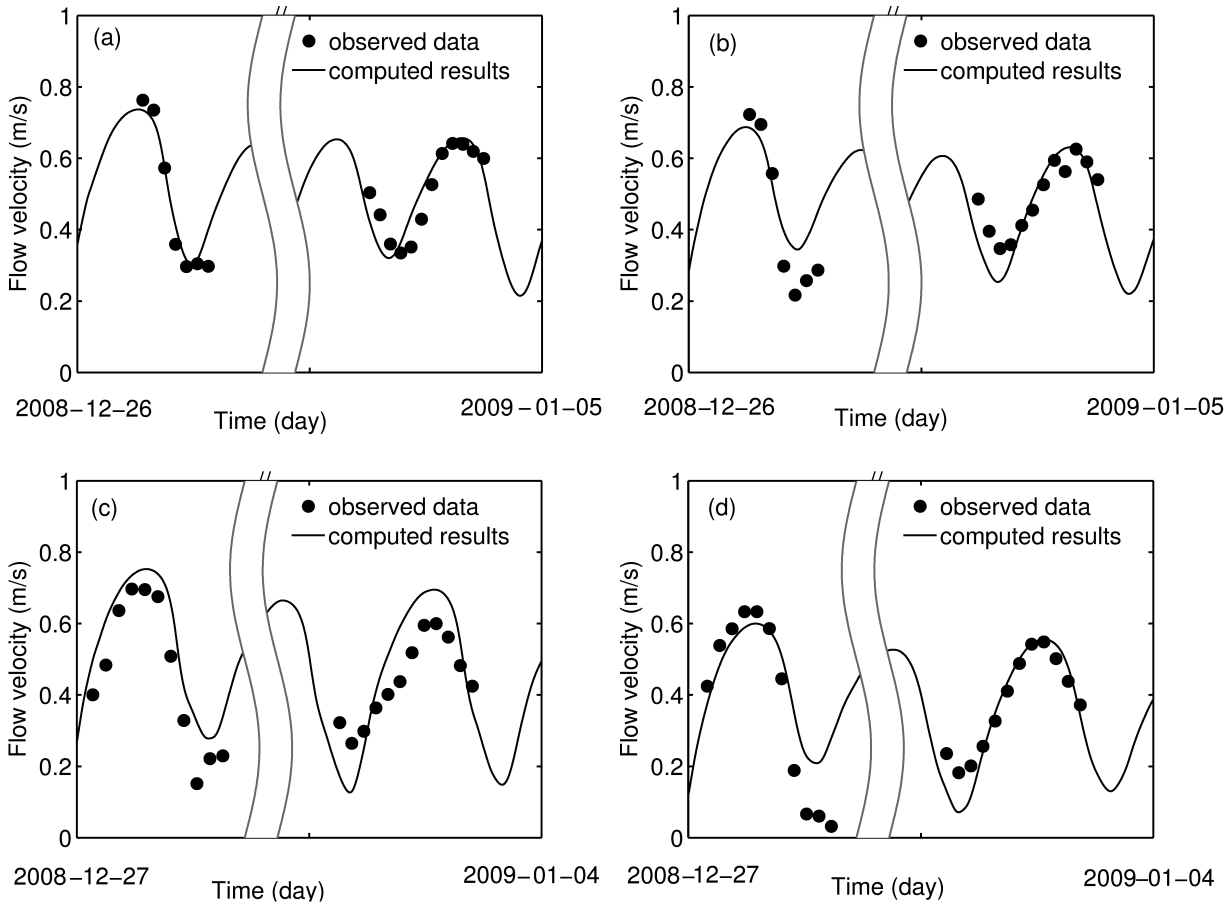

Fig. 10 Computed and measured flow velocity at: (a) DAN, (b) DAS, (c) FBN, and (d) FBS stations (Fig. 4) during the validation period. In each panel, observations in the left site were performed in spring tides while observations in the right site were performed in neap tides.

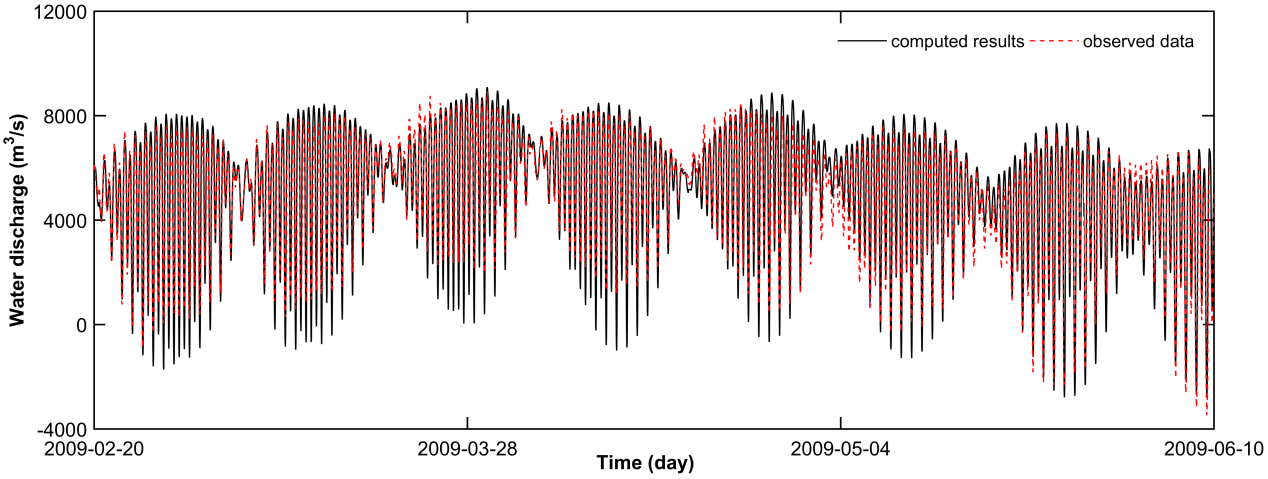

Fig. 11 Observed data and computed results of water discharge at Samarinda station, where positive water discharge coincides with seaward direction.

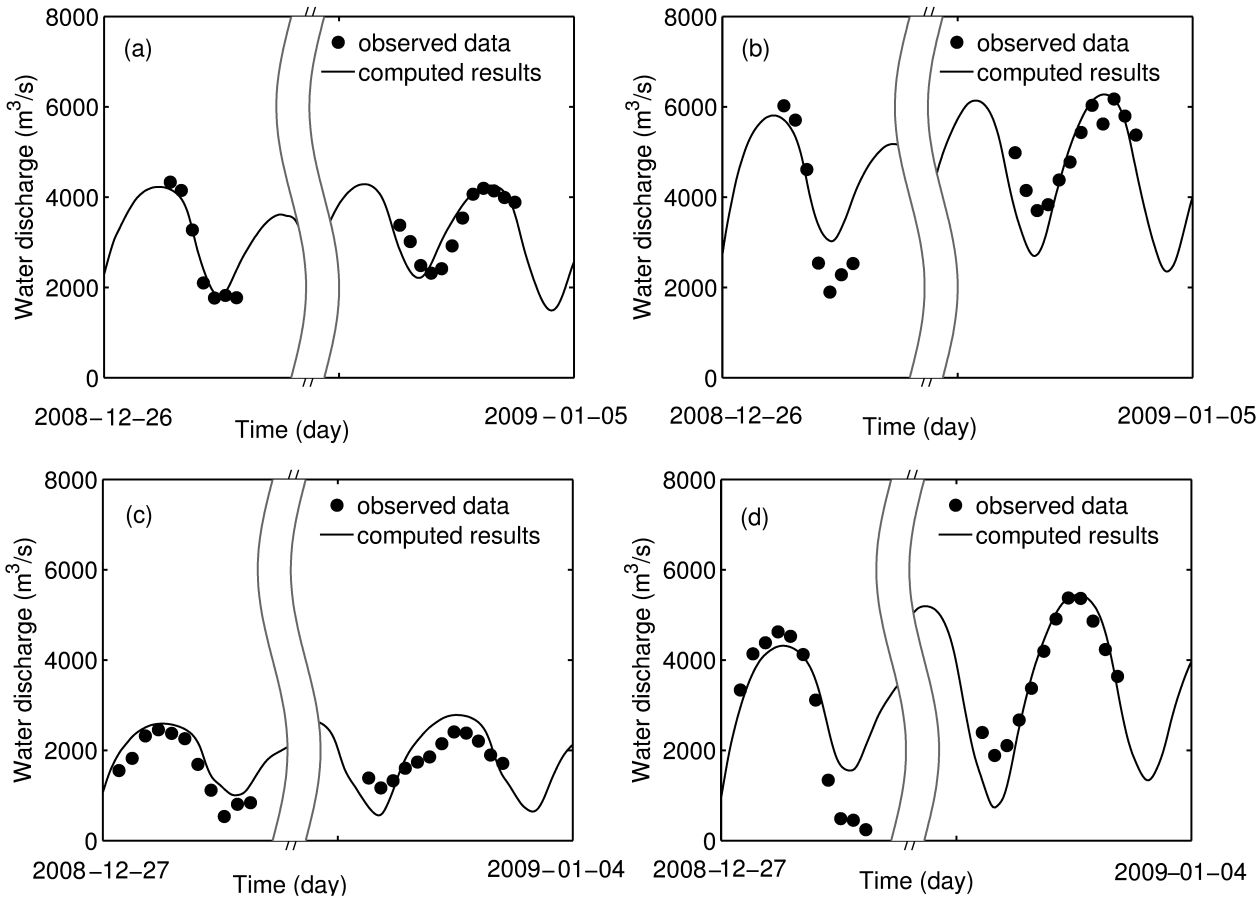

Fig. 12 Computed and measured water discharges at: (a) DAN, (b) DAS, (c) FBN, and (d) FBS stations (Fig. 4) during the validation period. In each panel, observations in the left hand site were performed in spring tides while observations in the right hand site were performed in neap tides.

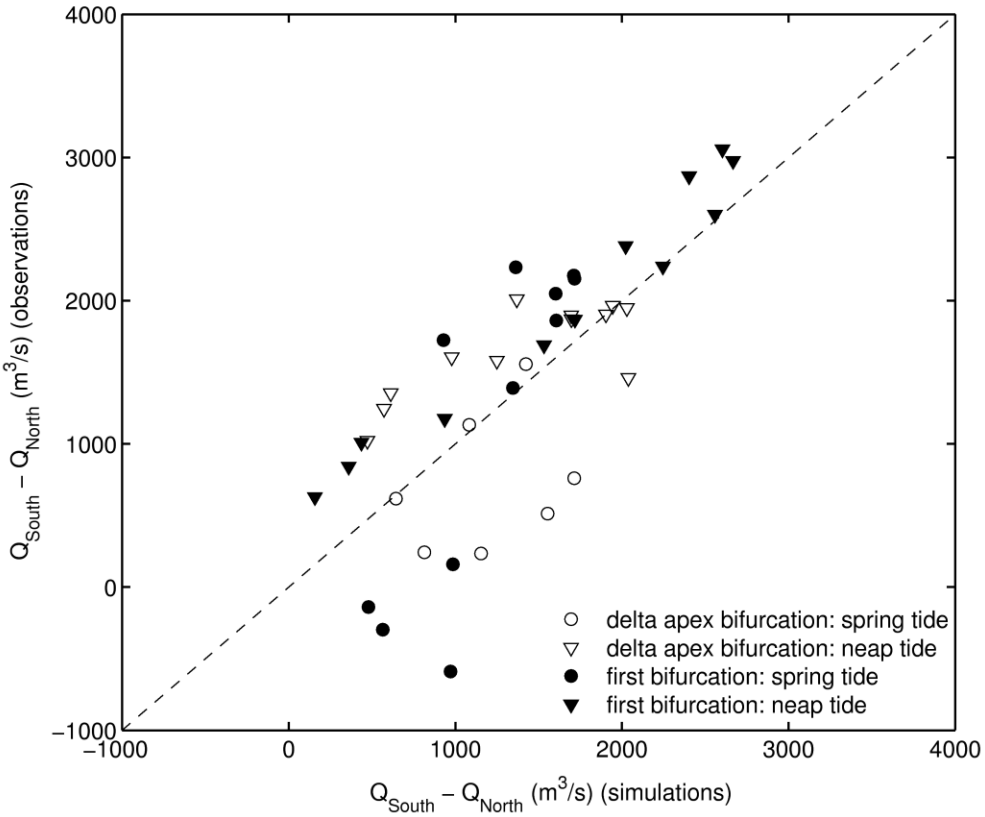

Fig. 13 Discharge difference between southern and northern channels obtained with the simulations and with observations. Each dot is calculated from the water discharge in the northern channel section (denoted by Q_{North}) and the water discharge in the southern channel section (denoted by Q_{South}). The quantity ($Q_{south} - Q_{north}$) in the vertical axis of the figure is calculated from the observation data while the one in the horizontal axis is computed from the numerical simulations.

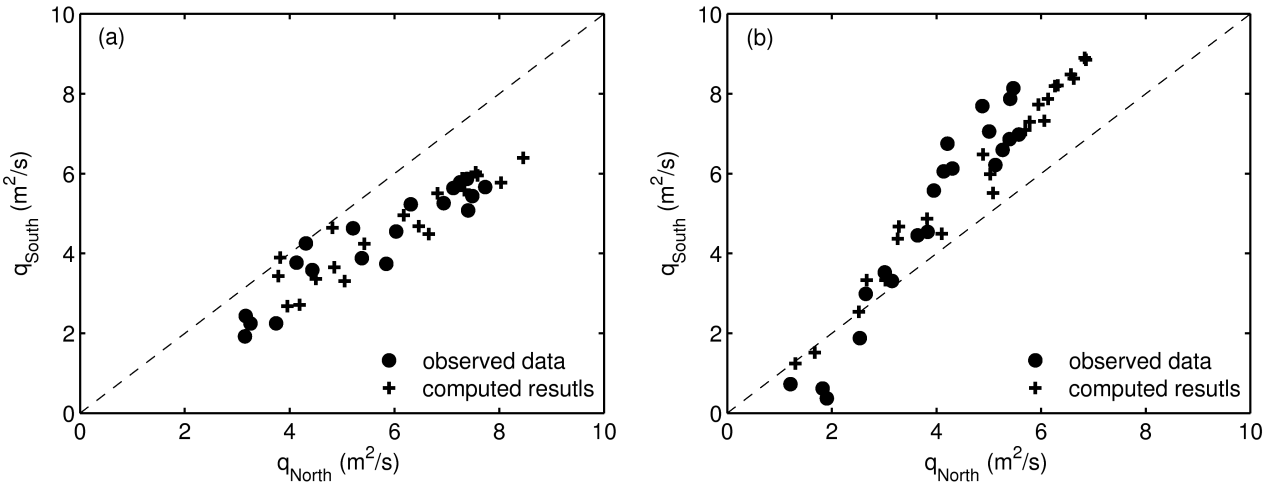

Fig. 14 Specific water discharge in the northern and southern channels at: (a) delta apex and (b) first bifurcations in the delta.

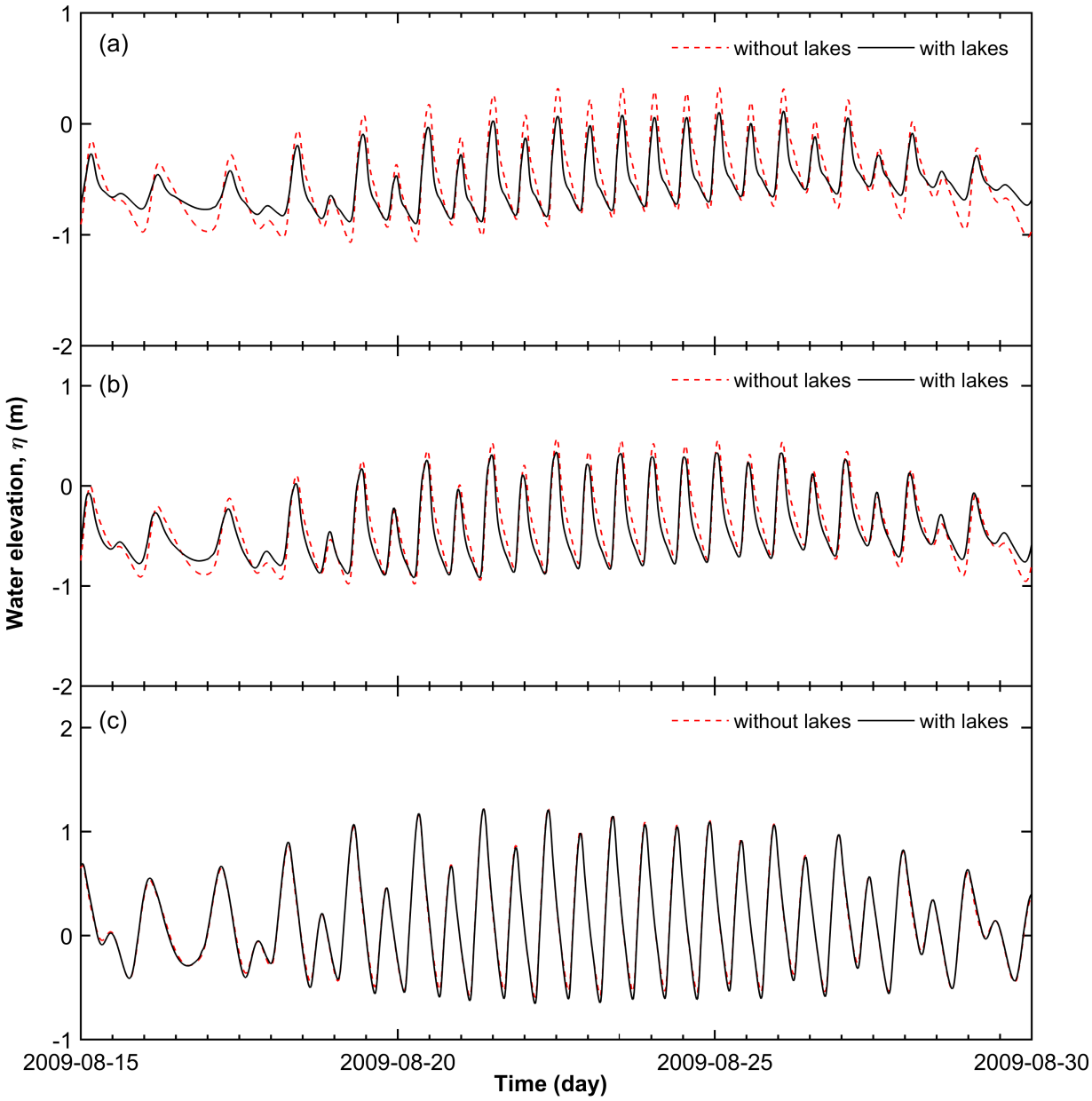

Fig. 15 Water elevation at: (a) Pela Mahakam, (b) Muara Karman, and (c) Samarinda, in the cases with and without the lakes.

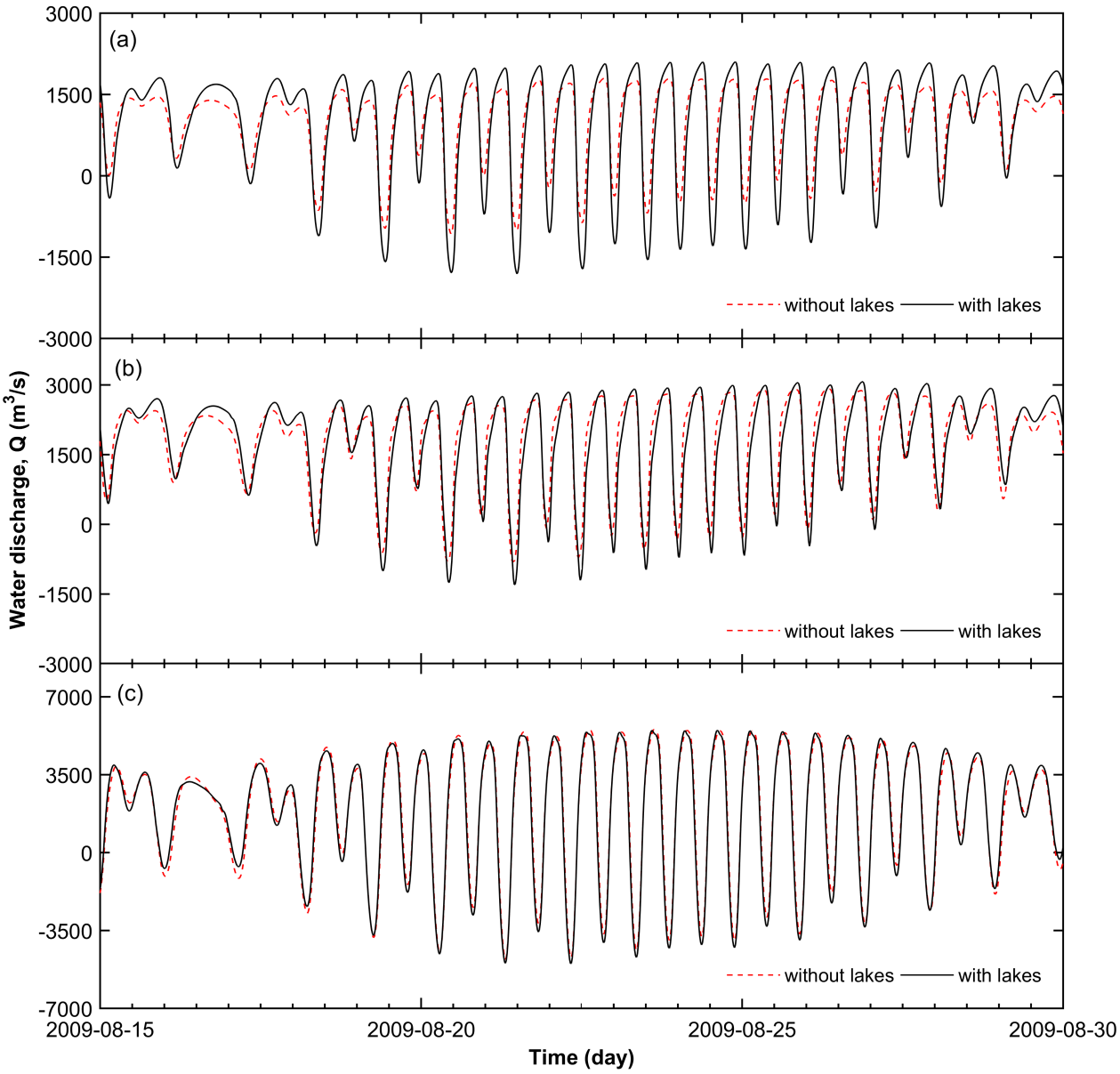

Fig. 16 Water discharge at: (a) Pela Mahakam, (b) Muara Karman, and (c) Samarinda, in the cases with and without the lakes. The positive water discharge coincides with the seaward direction.